Environmental Controls on the Tropical Island Diurnal Cycle in the Context of Intraseasonal Variability

MICHAEL B. NATOLI[a] AND ERIC D. MALONEY[a]

[a] *Colorado State University, Fort Collins, Colorado*

(Manuscript received 6 November 2022, in final form 18 July 2023, accepted 20 July 2023)

ABSTRACT: The mechanisms regulating the relationship between the tropical island diurnal cycle and large-scale modes of tropical variability such as the boreal summer intraseasonal oscillation (BSISO) are explored in observations and an idealized model. Specifically, the local environmental conditions associated with diurnal cycle variability are explored. Using Luzon Island in the northern Philippines as an observational test case, a novel probabilistic framework is applied to improve the understanding of diurnal cycle variability. High-amplitude diurnal cycle days tend to occur with weak to moderate offshore low-level wind and near to above average column moisture in the local environment. The transition from the BSISO suppressed phase to the active phase is most likely to produce the wind and moisture conditions supportive of a substantial diurnal cycle over western Luzon and the South China Sea (SCS). Thus, the impact of the BSISO on the local diurnal cycle can be understood in terms of the change in the probability of favorable environmental conditions. Idealized high-resolution 3D Cloud Model 1 (CM1) simulations driven by base states derived from BSISO composite profiles are able to reproduce several important features of the observed diurnal cycle variability with BSISO phase, including the strong, land-based diurnal cycle and offshore propagation in the transition phases. Background wind appears to be the primary variable controlling the diurnal cycle response, but ambient moisture distinctly reduces precipitation strength in the suppressed BSISO phase and enhances it in the active phase.

KEYWORDS: Maritime Continent; Madden-Julian oscillation; Monsoons; Statistics; Cloud resolving models; Diurnal effects

1. Introduction

The diurnal cycle is a primary contributor to total rainfall in the vicinity of tropical islands in the Maritime Continent (MC; Biasutti et al. 2012; Bergemann et al. 2015; Zhu et al. 2017; Ruppert and Chen 2020). Significant variability in the diurnal cycle is present from one day to the next, which provides opportunities to understand its nature (Houze et al. 1981; Chen and Takahashi 1995). Generally, convective precipitation on tropical islands tends to initiate in the late morning or early afternoon hours as a result of low-level convergence associated with the sea-breeze front or mountain–valley breezes (Saito et al. 2001; Mori et al. 2004; Kilpatrick et al. 2017). Convection can then organize and grow upscale, before occasionally propagating offshore into surrounding coastal waters after dark (Yang and Slingo 2001; Mapes et al. 2003; Sakurai et al. 2005). While the tropical island diurnal cycle has been studied extensively in its mean state or in a composite sense, much remains to be ascertained regarding its variability and behavior in response to changes in environmental conditions, including those produced by large-scale modes of tropical variability.

The largest source of tropical variability on intraseasonal time scales in the tropics is the Madden–Julian oscillation (MJO; Madden and Julian 1971, 1972). While the traditional boreal winter MJO is characterized by eastward propagation of enhanced convection from the Indian Ocean, across the MC, and into the west Pacific, this signal exhibits substantial northward propagation into the Asian monsoon region during boreal summer (Lawrence and Webster 2002; Wheeler and Hendon 2004; DeMott et al. 2013). This summertime mode, which has been identified as a modulator of active and break cycles in the monsoon, is often referred to as the boreal summer intraseasonal oscillation (BSISO; Lau and Chan 1986; Annamalai and Slingo 2001; Lee et al. 2013). The active MJO is expressed over oceans with strong westerly winds, ample moisture, and heavy rainfall, while the suppressed phase is characterized by weaker trade easterlies, a drier free troposphere, fewer clouds, and less rainfall with an oscillatory time scale of about 30–60 days (Madden and Julian 1994; Maloney and Hartmann 1998; Riley et al. 2011). The active BSISO operates on a similar timeline, and induces similar modulations

Supplemental information related to this paper is available at the Journals Online website: https://doi.org/10.1175/JCLI-D-22-0824.s1.

Corresponding author: Michael B. Natoli, mbnatoli@colostate.edu

DOI: 10.1175/JCLI-D-22-0824.1

of wind, moisture, cloud cover, and rainfall, but the envelope of active convection propagates northward in addition to eastward, often as a northwest to southeast oriented elongated band and dominates from June through October (Lau and Chan 1986; Annamalai and Slingo 2001). The BSISO has significant impacts on monsoon behavior in southeast Asia and the South China Sea, whereas the MJO mode is more prominent across Indonesia and northern Australia (Kikuchi et al. 2012). The MJO and BSISO can generally be considered to be the same phenomenon that exists in a different seasonal background state (e.g., Jiang et al. 2018; Wang and Sobel 2022). While the review of the literature in this section will use the term MJO due to the much greater attention the boreal winter mode has received in prior research, our new results below will use the term BSISO in accordance with a focus on the boreal summer season and the test case of Luzon in the northern Philippines.

An understanding of diurnal precipitation behavior associated with a passing MJO event over islands in the MC remains incomplete. In studies of several different islands in varying seasons, many have found a tendency for the most intense diurnal cycles to occur during the suppressed MJO phase (Sui and Lau 1992; Ho et al. 2008; Rauniyar and Walsh 2011; Oh et al. 2012; Xu and Rutledge 2018), although a diurnal cycle with a late afternoon peak is still present in the active phase (Chen and Takahashi 1995; Chudler et al. 2020). Subsequent research has taken a more precise look at the diurnal cycle during an MJO life cycle and identified the late suppressed period and transition to active as producing the most favorable large-scale conditions for a strong diurnal cycle over land (Peatman et al. 2014; Natoli and Maloney 2019). In a Weather Research and Forecasting (WRF) Model simulation, Vincent and Lane (2017) also found this peak in the diurnal cycle during the transition to MJO active convection phases, with a secondary peak in the reverse transition.

An understanding of the mechanism regulating this diurnal cycle behavior has not yet been convincingly established. Some have pointed to increased solar radiation owing to the reduced cloud cover as the reason for high amplitude diurnal cycles to occur in the suppressed MJO phase (e.g., Peatman et al. 2014; Birch et al. 2016), but this would not explain the preference for the strongest diurnal cycles to occur in the late suppressed and transition to active MJO phases. Peatman et al. (2014) proposed that frictional moisture convergence associated with the Kelvin wave to the east of MJO convection (Gill 1980) could be important for enhancing the diurnal cycle. Later budget analysis suggested a more general role for moisture convergence in supporting diurnal convection, namely the convergence of MJO-scale moisture by diurnal-scale winds (Chen et al. 2019; Lu et al. 2019). Free tropospheric moisture availability has been shown to be an important control on tropical precipitation and its diurnal cycle (Bretherton et al. 2004; Vincent and Lane 2017). The wind profile, especially in the lower troposphere, has also been identified as an important factor. Specifically, the strong winds in the MJO active phase reduce the land–sea contrast and thus daytime convection over land (Shige et al. 2017; Wang and Sobel 2017; Wu et al. 2017, 2018; Yokoi et al. 2019; Natoli and Maloney 2023). Conversely, light winds tend to favor a substantial diurnal cycle on the leeward side of islands (Virts et al. 2013; Short et al. 2019; Qian 2020; Natoli and Maloney 2021). Since MJO moisture leads the strong westerly winds in phase (Maloney and Hartmann 1998), considering the details of the phase relationship between the MJO wind and moisture variations presents a compelling hypothesis to explain this diurnal cycle behavior over an MJO life cycle. The presence of light easterly winds, increasing ambient moisture, and sufficient insolation in the transition from MJO suppressed to active conditions could explain the strong offshore propagating diurnal cycle on the western shore of MC islands.

This study seeks to test the previously stated hypothesis through a rigorous, probabilistic analysis of observational data and tightly controlled idealized model simulations. We aim to clearly establish which environmental conditions impact the local diurnal cycle. These conditions could be induced by the MJO or other modes of large-scale tropical convective variability such as the quasi-biweekly oscillation (Chen and Chen 1995; Natoli and Maloney 2021) or various equatorial waves (Ferrett et al. 2019). The mechanisms through which the MJO modulates these environmental conditions, and how exactly these environmental conditions impact the diurnal cycle, are beyond the scope of this paper, but information on these topics can be found in the existing body of literature (e.g., Holloway and Neelin 2009; Sobel and Maloney 2013; Natoli and Maloney 2023; as well as numerous others, some of which are discussed above). The piece of the puzzle presented by this study is an improved understanding of how local environmental conditions impact the diurnal cycle, which helps to better explain the BSISO–diurnal cycle relationship. In the next section, we will outline the datasets and methods employed, as well as provide a detailed description of the model setup. The observational results will be discussed in section 3 through a probabilistic framework that includes the range of conditions possible within a certain BSISO phase in order to understand how certain BSISO phases make environmental conditions that favor a strong diurnal cycle more likely. In section 4, numerous model simulations using a 3D version of Cloud Model 1 designed to explicitly test our hypothesis will be discussed. These simulations will modify the base state according to BSISO composite profiles, and then attempt to isolate the environmental conditions responsible for the observed BSISO modulation of the diurnal cycle. Last, the main conclusions and implications of these results will be explained in section 5.

2. Data and methods

a. *Observations*

Satellite observations and reanalysis are studied for the period of June–September (JJAS) 1998–2020. Precipitation estimates from version 1.0 of the bias-corrected Climate Prediction Center Morphing Technique (CMORPH; Joyce et al. 2004; Xie et al. 2017) are derived from multiple satellites and are available at 8-km spatial and 30-min temporal resolution. Reanalysis data from the fifth-generation reanalysis by the European Centre for

Medium-Range Weather Forecasts (ERA5; C3S2017; Hersbach et al. 2020) is used at 0.25° spatial and hourly temporal resolution for both observational analysis and driving the model described below. Variables examined on pressure levels from 1000 to 100 hPa include zonal wind, specific humidity, geopotential height, and temperature. Total column water vapor (TCWV) and surface downward shortwave radiation (insolation) are also analyzed. Additional ERA5 variables are used in the model setup and are described below. Topographic information from the NOAA ETOPO2 dataset (National Geophysical Data Center 2006) provides geographical context for the observational results.

CMORPH precipitation and ERA5 vertical profiles are composited based on the phase of the BSISO as defined by Lee et al. (2013), which is constructed from the first two multivariate EOFs of outgoing longwave radiation and 850-hPa zonal wind during boreal summer in the Asian monsoon region. Days in JJAS are only included in the composite if the amplitude of the BSISO index was greater than 1.0, and then data are partitioned into one of eight phases. The distribution of the CMORPH precipitation diurnal cycle amplitude among all days in the study period is frequently referenced as a baseline. The diurnal cycle amplitude (DCA) is defined in this study as the difference between the daily maximum spatially averaged precipitation rate and the daily minimum spatially averaged precipitation rate. This is done for six averaging domains inside boxes A–F shown in Fig. 1. Thus, a DCA is found for each box, for each of the 2806 days in JJAS 1998–2020. The 85th percentile DCA is calculated for each box as a proxy for a day on which a strong precipitation diurnal cycle was observed. Other percentile thresholds were also considered, and the 85th percentile was found to be an appropriate balance between capturing only the most significant diurnal cycle events, while also retaining a substantial sample size. The results were qualitatively insensitive to the precise choice of percentile threshold. Days on which the DCA exceeded the 85th percentile in each box are referred to as 85th percentile diurnal cycle amplitude (DCA85) days. Note that specific dates included in the DCA85 group will be different for each averaging box.

Statistical significance is shown in this study with a bootstrap method. Since by definition, the total distribution of environmental conditions on DCA85 days is 15% of the total number of JJAS days in the 23-yr study period (2806 days), 1000 random samples of 420 days are collected and compared against the DCA85 day distributions. Another 1000 random samples were collected in order to assess the statistical significance of BSISO samples. These were made of 63 *independent* samples (the lowest number of independent samples for any of the 8 phases), with a number of successive days following the randomly selected date also included based on a Poisson distribution. This was done because the BSISO tends to remain in the same phase for several consecutive days, so the total number of days in a certain BSISO phase is not a truly independent sample. More details on this method can be found in Natoli and Maloney (2019).

This study uses Luzon Island in the northern Philippines as a test case for both the observational and modeling components.

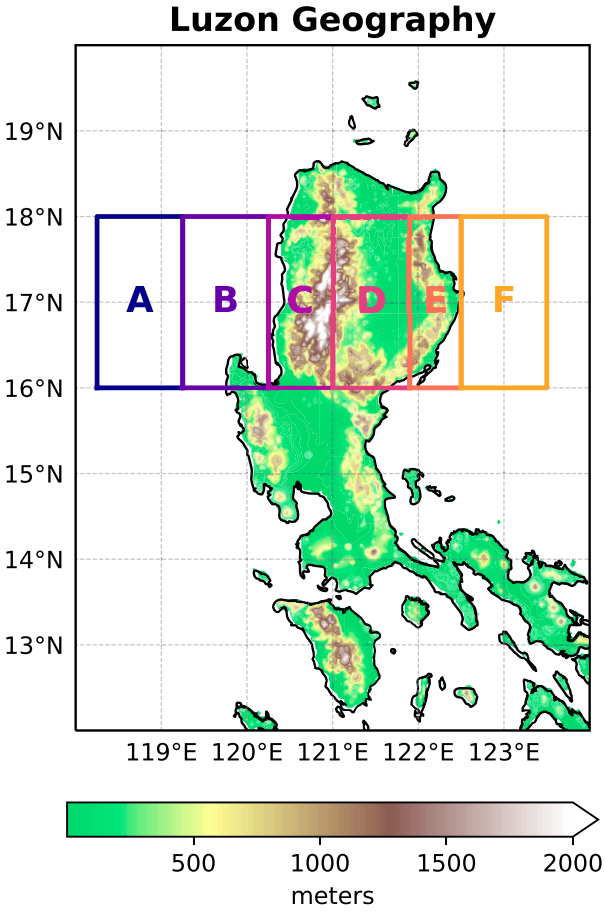

FIG. 1. (a) NOAA ETOPO2 Topography (m) over the northern Philippines, overlaid with boxes of spatial averaging used in this study.

The diurnal cycle in the Indonesian MC has received considerably more attention in the current body of literature than that in the Philippines and the Asian monsoon region, particularly in the context of intraseasonal variability. However, substantial diurnal cycle variability associated with the BSISO and/or active and break periods of the monsoon flow has been identified in the Philippines (e.g., Park et al. 2011; Xu and Rutledge 2018; Natoli and Maloney 2019, among others). Thus, this region presents a compelling case study to expand the body of knowledge to different regions of the tropical warm pool. Since Luzon Island contains the largest population center of the Philippines, and holds fairly convenient geography for a comparison to an idealized model (e.g., more or less north-to-south oriented coastlines and coastal mountain ranges), this island was chosen as the test case for this study.

b. *CM1 setup*

1) CONTROL

Idealized modeling experiments are conducted using version 20.2 of Cloud Model 1 (CM1; Bryan and Fritsch 2002) in order to examine the sensitivity of diurnal cycle behavior to

the BSISO base state, and the sensitivity to single environmental variables in isolation. The fairly low computational cost of this model facilitates the numerous experiments discussed in this manuscript. The model is run at 1-km horizontal grid spacing with a domain size of 800 km zonally, 60 km meridionally, and 20 km vertically. The high horizontal resolution allows for explicit simulation of convection. A stretched vertical grid is used, with grid spacing of 50 m in the boundary layer, increasing to 1150 m at the model top. In each experiment, the model is iterated for 7 days, with output saved every 30 min.

Boundary conditions are open radiative on the east and west boundaries, periodic at the north and south boundaries, free-slip at the top boundary, and partial-slip (includes a coefficient of friction) at the bottom boundary. To simulate the diurnal cycle in initial experiments, a 200-km-wide island (roughly the width of Luzon Island between 16° and 18°N as shown in Fig. 1) is placed at the center of the domain. The island is uniform in the meridional direction, which makes this more of a quasi-3D simulation. The physical setup is similar to Wang and Sobel (2017) and allows for the advantages of 3D cloud dynamics while easing analysis and maintaining a fairly small domain to reduce computational cost. The model simulations were designed to be as simple as possible, while still replicating the effects on the diurnal cycle of ambient wind and moisture seen in observations. This was qualitatively achieved without topography, so therefore it was not included in our simulations for simplicity. Riley Dellaripa et al. (2020) simulated the diurnal cycle over Luzon in a convection-permitting regional model and showed that results are qualitatively similar when topography is removed. They demonstrated relatively minor differences, mostly in local spatial organization of convection, with and without topography during a simulated BSISO event. Additionally, Ruppert and Chen (2020) found that topography is important for explaining the precise location of mean rainfall maximum within an island, but not for explaining island-scale or larger precipitation. In simulations of the MC with and without topography, Ruppert et al. (2020) noted that its inclusion is only of secondary importance to offshore gravity wave propagation. These results together justify the decision in this study to use flat topography to explore the environmental conditions important for the local diurnal cycle in the simplest possible framework.

The base state for each simulation comes from ERA5 vertical profiles averaged inside the region spanning boxes A–F (Fig. 1). The control simulations in this study are a set of eight simulations with the base state varying with the BSISO composite environmental profile. The background zonal wind and anomalous moisture profiles used in each of these simulations are shown in Fig. 2. In addition to moisture and zonal wind, the BSISO composite temperature profile is also varied along with values of mean sea level pressure (MSLP) and T2m. Initial surface conditions come from the ERA5 sea surface temperature (SST) and the ERA5 skin temperature from land points below 400 m in elevation. The land surface temperature is allowed to evolve freely, while the SST is fixed at the ERA5 mean value of 302.5 K. The model is initialized with insolation corresponding to 0500 local time (LT) at 17°N on 1 August. This initialization was chosen to provide the best comparison to the observational analysis of this manuscript, which focuses on Luzon Island during the JJAS season. Thus, a start time just before sunrise in roughly the middle of the study period was ideal.

The base state is maintained through two methods. First, the inflow at the lateral boundaries is nudged toward the base state with a time scale of one minute. Second, a large-scale nudging technique is applied, in which the domain mean of zonal wind, water vapor mixing ratio, and potential temperature at each vertical level is nudged back to the base state with a time scale of 3 h. This time scale was found to be a relatively good balance between preventing progressive divergence from the base state late in the simulation and free evolution of the model diurnal cycle. The following parameterizations are utilized: a revised surface scheme from the Weather Research and Forecasting (WRF) Model (Jiménez et al. 2012), the Yonsei University planetary boundary layer (PBL) scheme (Hong et al. 2006), the Morrison double-moment microphysical scheme (Bryan and Morrison 2012), and the NASA-Goddard radiation scheme adapted to CM1 from the Advanced Regional Prediction System model. A Rayleigh damping layer is applied above 15 km with an *e*-folding time scale of 5 min. In all experiments in this study, very small random perturbations are applied to the initial condition to introduce some 3D inhomogeneity.

2) Sensitivity experiments

A series of sensitivity experiments alters the model base state to isolate the impacts of ambient moisture and lower tropospheric winds on the diurnal cycle. These variables are often invoked to explain the BSISO–diurnal cycle relationship (Vincent and Lane 2017; Natoli and Maloney 2019, 2021; Sakaeda et al. 2020; Peatman et al. 2021). The first eight simulations of this group titled "BSISO Wind Only" are designed to examine diurnal cycle behavior attributable to the wind anomalies associated with different BSISO phases, in the absence of other confounding factors. A more detailed analysis on the impact of the wind on the tropical island diurnal cycle can be found in Natoli and Maloney (2023). In these experiments, only the BSISO composite zonal wind profile is used in the model base state, while the JJAS mean vertical profiles are used for all other variables.

Moisture experiments contribute an additional eight sensitivity tests. The base-state moisture is varied across four set values while the temperature profile comes from the JJAS mean. Each moisture level is run twice, once with BSISO phase 3 composite winds (light to moderate easterlies) and once with BSISO phase 7 composite winds (strong westerlies), yielding a total of eight simulations. The highest moisture experiment ($+1.5\sigma$) uses a moisture profile from a composite of JJAS days in which the TCWV was between 1.25 and 1.75 standard deviations above the JJAS mean. Next, we use BSISO composite phase 7 moisture (P7), followed by BSISO composite phase 3 moisture (P3) profiles (Fig. 2b). The driest (-1.5σ) comes from days on which TCWV was between 1.25 and 1.75 standard deviations below the JJAS mean. The

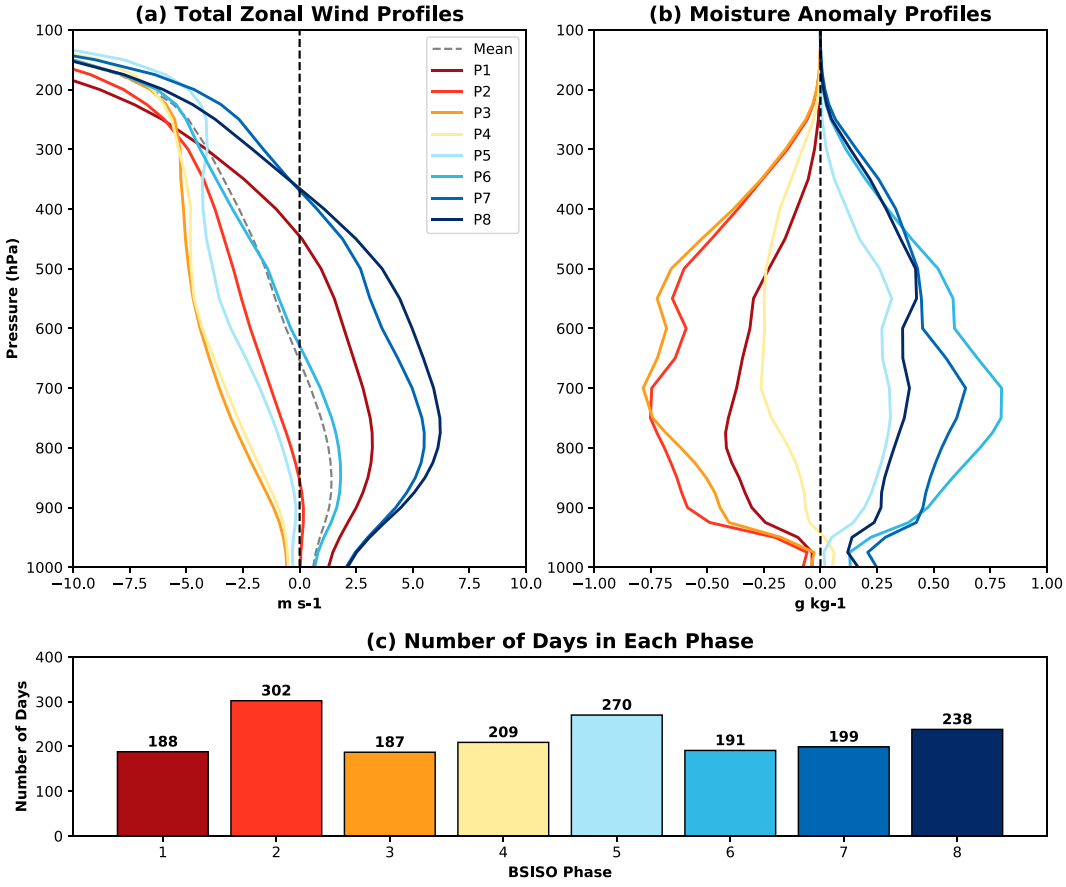

FIG. 2. (a) Composite ERA5 zonal wind profiles (m s^{-1}) for each BSISO phase in JJAS 1998–2020. Values are averaged inside boxes A–F together (Fig. 1a). The dashed gray line indicates the mean profile from all JJAS days. (b) Anomalous moisture profiles (g kg^{-1}) by BSISO phase. (c) The number of JJAS 1998–2020 days that fall into each bin is shown as bars, with this number noted on top.

highest and lowest moisture experiments serve to test a more extreme case than what can be obtained with just the BSISO composite moisture values. Note that the P7 moisture experiment with phase 7 winds is very similar to the phase 7 control experiment, but not identical, only varying in the temperature profile which comes from the JJAS mean in the moisture experiments compared to the BSISO composite in the control.

A brief summary of each of the simulations described in this study is shown in Table 1.

3. Observations

The goal of this section is to clearly elucidate the environmental background conditions associated with high-amplitude diurnal cycles near Luzon. While most studies evaluating the relationship between the MJO/BSISO and the diurnal cycle approach the problem through composites of precipitation based on the large-scale feature (e.g., Rauniyar and Walsh 2011; Peatman et al. 2014; Lu et al. 2019; Natoli and Maloney 2019, among others), a reverse approach is taken here. In particular, we highlight the days on which a high-amplitude diurnal cycle occurs, and identify the anomalous environmental conditions associated with these days. It is then demonstrated that certain BSISO regimes make specific configurations of local environmental background conditions that favor strong diurnal cycles significantly more likely. This analysis utilizes a probabilistic approach toward the understanding of ISO–diurnal cycle interactions.

TABLE 1. Summary of CM1 simulations examined in this study.

Title of set	No. of simulations	Parameter altered	Wind profile used
Control	8	Base-state profile (all variables)	All BSISO phases
Wind Only	8	Base-state wind profile	All BSISO phases
Moisture	8	Base-state moisture profile	BSISO phases 3 and 7

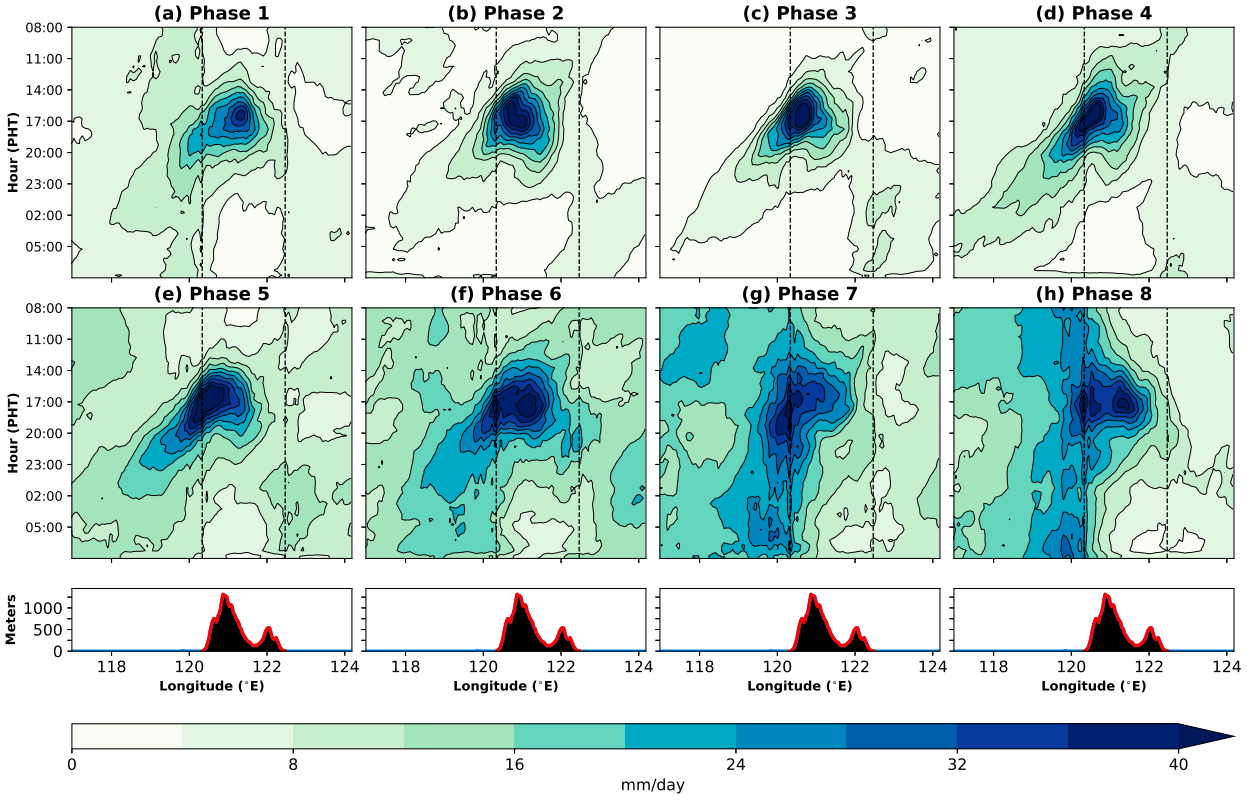

FIG. 3. Hovmöller diagrams of CMORPH composite precipitation rate (mm day^{-1}) on JJAS days by Lee et al.'s (2013) BSISO index. Results are averaged across latitude inside boxes A–F (Fig. 1a), but additional longitude to the west of Box A and the east of box F is also included. Time starts at 0800 local time in each panel and increases downward. Vertical dashed lines show the position of each coastline. The average topography from NOAA ETOPO2 inside boxes A–F is shown at the bottom for reference.

A more thorough analysis of the impact of the BSISO on the Luzon diurnal cycle can be found in Natoli and Maloney (2019) but is briefly reviewed here. Figure 3 shows Hovmöller diagrams of composite diurnal cycles of CMORPH precipitation estimates using Lee et al.'s (2013) BSISO phases. We note that Fig. 3 is very similar to Fig. 7a of Natoli and Maloney (2019), but not identical since we restrict our study here to JJAS rather than May–October. This is averaged across the latitudinal domain of boxes A–F in Fig. 1 but includes a slightly expanded longitudinal range. Convection initiates near the western shore in the mid- to late afternoon and exhibits westward offshore propagation into the South China Sea (SCS) in most phases. The diurnal cycle is much more pronounced in the suppressed BSISO phases (2–4), compared to the active phases (6–8). In particular, the transition from suppressed to active conditions through phases 3, 4, and 5 tends to exhibit the strongest diurnal cycles with the best westward propagation. This behavior has been hypothesized to be due to the combination of easterly wind anomalies and sufficient moisture and insolation that are concurrent in this transition (Natoli and Maloney 2019, 2021). Natoli and Maloney (2023) also showed that westward propagation is highly sensitive to the background wind profile.

Figure 4 provides a closer look at the diurnal cycle in each of the boxes A–F in Fig. 1. Composite diurnal cycles spatially averaged inside each box are shown for all JJAS days in blue, while the composite for DCA85 days is shown in red. A histogram also shows the time at which the maximum daily precipitation rate occurs for all JJAS days. The land boxes (C, D, and E) show a strong preference for the diurnal cycle to peak during the late afternoon, around 1700 LT, although it is more pronounced for the west (box C) and center (box D) of Luzon compared to the east (box E). The coastal South China Sea (b) shows a significant preference for a diurnal cycle peak around 2000, consistent with offshore propagation. While the histograms for the boxes farther offshore (e.g., boxes A and F) do not show a clear preference for the diurnal cycle to peak at a certain time among all JJAS days, filtering for only DCA85 days clearly shows a peak around midnight in box A, and around 0200 LT in box F. It is likely that when a strong diurnal cycle is observed offshore, it is associated with convection that initiated over land in the late afternoon and then propagated offshore (Chudler et al. 2020).

The probability of observing a DCA85 day within a given BSISO phase for each subregion is shown in Fig. 5. Since a DCA85 day has by definition a 15% chance of occurring, a relative change of +50% in Fig. 5 would indicate that given the BSISO is active in that specific phase, with a 22.5% chance for a DCA85 day. On the west coast (box C), there is a small increase in the probability of a DCA85 day during

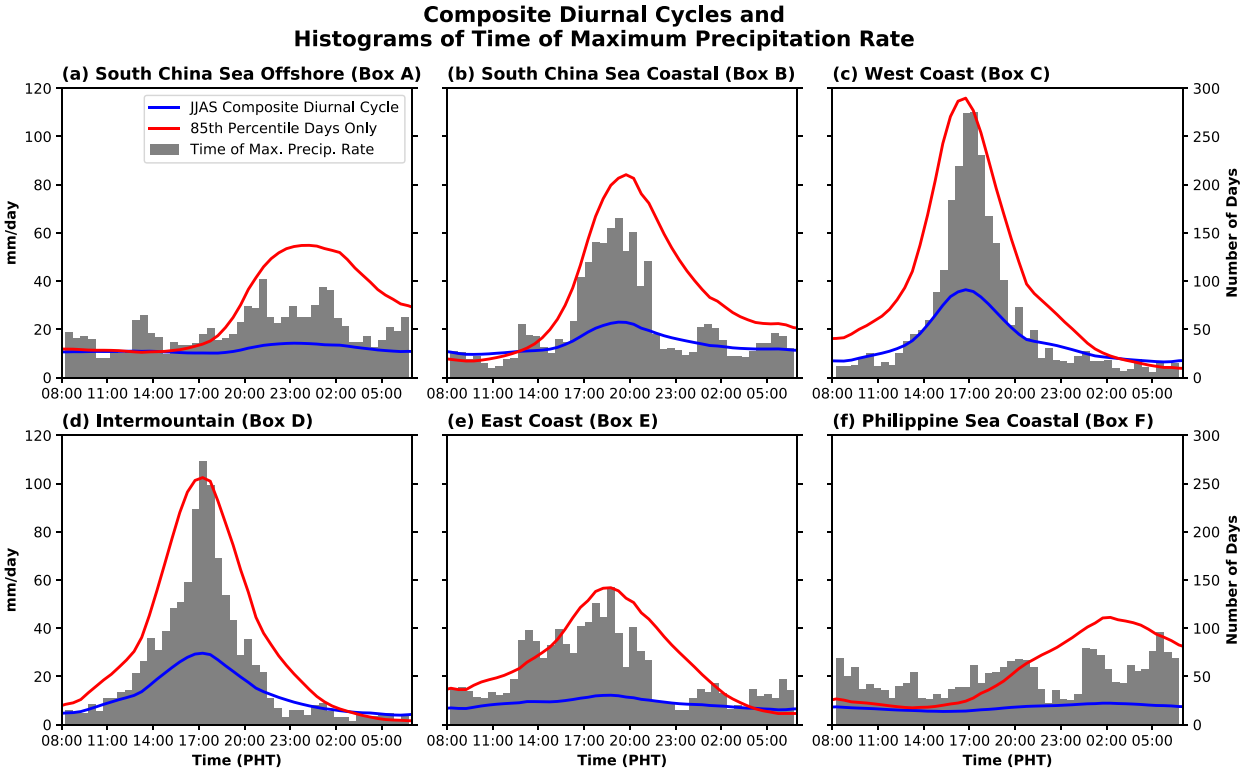

FIG. 4. The composite diurnal cycle of CMORPH precipitation (mm day^{-1}) averaged inside each box on all JJAS 1998–2020 days in Fig. 1 (blue line). The composite diurnal cycle only from days on which the amplitude of the diurnal cycle (as defined by the difference between daily maximum precipitation and daily minimum precipitation rate) is greater than its 85th percentile (red line). This includes 420 days. A histogram showing the number of days on which the maximum precipitation rate occurs in each half-hour bin (gray). The first (2330–0000 UTC or 0730–0800 local time) and last (0000–0030 UTC or 0800–0830 LT) bins are excluded since those bins capture days on which precipitation is either increasing or decreasing through the whole day due to longer time-scale features. Boxes C–E include mainly land points, while boxes A, B, and F include mainly oceanic points.

phases 2–5, consistent with the composite analysis (Fig. 3). Interestingly, the central and eastern portions of the island tend to have a reduced probability of a strong diurnal cycle during these phases. The east coast (box E) exhibits higher probabilities for DCA85 days during phases 6–8. Offshore, each box (A, B, and F) is more likely to see a DCA85 day given the BSISO in phases 5 or 6, close to phases 4 and 5, which were identified by Natoli and Maloney (2019) with composite analysis as the phases with the most robust offshore propagation. The consistency between the east and west side of the island is somewhat surprising. However, based on the later timing of the diurnal cycle peak in box F (Fig. 4f) and the discontinuous increase in precipitation off the eastern coastline in the Hovmöllers of Figs. 3e and 3f, we speculate that the diurnal cycle in the coastal Philippine Sea to the east of Luzon is driven by the land breeze and is independent from land-based precipitation, unlike that on the west side of Luzon. Overall, the probabilistic results here are consistent with prior studies showing the preference for strong diurnal cycles during the suppressed BSISO phases over the west coast, with offshore propagation particularly favored during the transition from suppressed to active phases (Xu and Rutledge 2018; Xu et al. 2021; Natoli and Maloney 2019; Chudler et al. 2020).

Next, the environmental background conditions present on DCA85 days will be considered. Here, we examine fields from ERA5 averaged across boxes A–F (Fig. 1) to diagnose the larger-scale environment. Figure 6 shows histograms of three different variables hypothesized by prior studies (e.g., Vincent and Lane 2016; Yanase et al. 2017; Natoli and Maloney 2019, 2021; Short et al. 2019) to be important for modulating the local diurnal cycle. For the sake of brevity, the results for only two of the six boxes in Fig. 1 are shown, although the results from the other boxes are similar. In each panel, the gray bars display the histogram of one environmental variable from all JJAS days. The colored bars superimposed show the distribution when only DCA85 days in the box (coastal SCS/box B for left column, east coast/box E for right column) are considered. While not shown in the figure, it was confirmed via a bootstrap analysis that each of the six distributions based on DCA85 days shown in color in Fig. 6 have statistically significant differences (at the 95% confidence level) in their means compared to their underlying full distributions shown in gray.

Stark stratification is seen in 850-hPa zonal wind (u850) (Figs. 6a,d). While the distribution from all JJAS days is fairly well centered around 0 m s^{-1} with a slight positive skew,

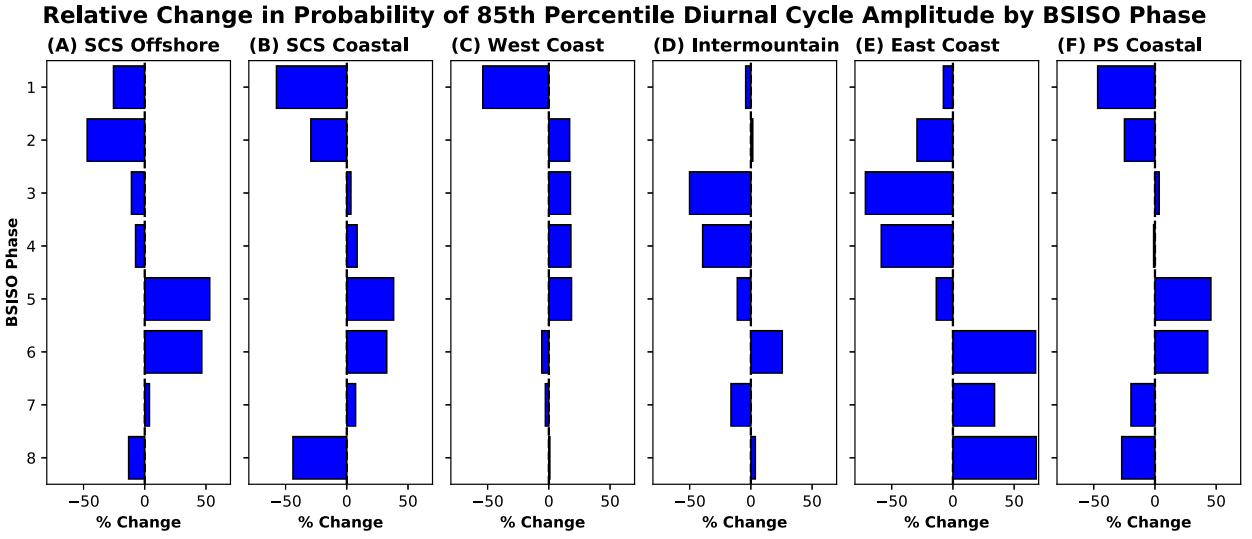

FIG. 5. The relative change in the probability of an 85th percentile diurnal cycle amplitude day occurring in each box from Fig. 1 given a specific BSISO phase (*y* axis). For example, if 30% of BSISO phase *X* days showed an 85th percentile diurnal cycle amplitude in box *Y*, it would display as a 100% increase, since 15% of all days can be expected to exceed the 85th percentile. There are 420 DCA85 days for each subregion.

DCA85 days in the coastal SCS are strongly preferred with a weak easterly wind. While they can occur with a westerly wind, the probability is sharply reduced given the presence of a westerly wind in the lower troposphere. Conversely, DCA85 days on the east coast are substantially *less* likely with an easterly wind, and become favored with a weak to moderate westerly wind. This indicates that a high-amplitude diurnal cycle becomes much more likely given the presence of a weak to moderate offshore background wind. Similarly conspicuous separation is apparent in TCWV. DCA85 days are much more likely in both boxes given a higher than average TCWV. This is unsurprising given previous studies that show a close correlation between precipitation and free tropospheric moisture in the tropics (e.g., Bretherton et al. 2004; Holloway and Neelin 2009, 2010; Kuo et al. 2017). Isolating the contributions of surface shortwave variations to the diurnal cycle is slightly more complicated. To reduce the influence of cloud cover induced by the diurnally generated convection itself, we consider only morning insolation by taking the average downward surface shortwave for 0600–1200 LT. The results in Figs. 6c and 6f are somewhat unexpected. The distribution of morning insolation for DCA85 days in both subregions is noticeably *lower* than the distribution for all JJAS days. In other words, a DCA85 day becomes less likely given higher insolation in the morning, but confounding variables are almost certainly present. We hypothesize that low moisture days, which clearly favor a suppressed diurnal cycle (Figs. 4b,e), are also associated with reduced cloudiness and thus higher insolation. In fact, the time series of daily TCWV and morning insolation used here are negatively correlated with $R^2 = 0.49$. This is substantially higher than the correlation of u850 with TCWV or morning insolation, which yield R^2 values of 0.14 and 0.26 respectively. The lack of moisture on such unusually sunny days appears to be a more significant factor for suppressing the diurnal cycle. This analysis suggests that the influence of insolation on the diurnal cycle is subdued compared to the effect of background moisture and low-level zonal wind.

To tie the above discussion together, 2D histograms of TCWV and u850 are considered to show that certain background states of wind and moisture lead to strong diurnal cycles. Subsequently, it will be shown that certain BSISO phases make such conditions more likely. Figure 7 shows the 2D histogram based on the daily average values of these two variables for all JJAS days in contours. The anomaly in the histogram given the occurrence of a DCA85 day is shown as colors. Anomalies are determined by first calculating the 2D histogram of wind and moisture only on DCA85 days, and then scaling those values as if the sample size were the same for DCA85 days and all JJAS days (e.g., the DCA85 histogram is divided by 0.15). Finally, the difference is calculated and displayed. Bins that contain values statistically different from the full distribution of 23 years of JJAS days at the 95% confidence level via a bootstrap method have a small white dot in their center. This demonstrates that there is a 5% or less probability that the anomaly in that bin resulted from purely random chance. On the west coast of Luzon (Fig. 7c), DCA85 days are considerably more likely when TCWV is near to above average, and u850 is weakly easterly. DCA85 days in central Luzon (Fig. 7d) are favored again with near to above average TCWV, and near zero to weakly westerly u850. The placement of higher probabilities indicates noticeably more westerly winds than the west coast, while strong winds of either sign appear to diminish the diurnal cycle. The east coast (Fig. 7e) distribution shifts further toward westerly wind and higher moisture, occupying mostly the upper right quadrant. A similar story can be derived from the offshore boxes (Figs. 7a,b,f). In each offshore subregion, DCA85 days occur preferentially with near to above average moisture and

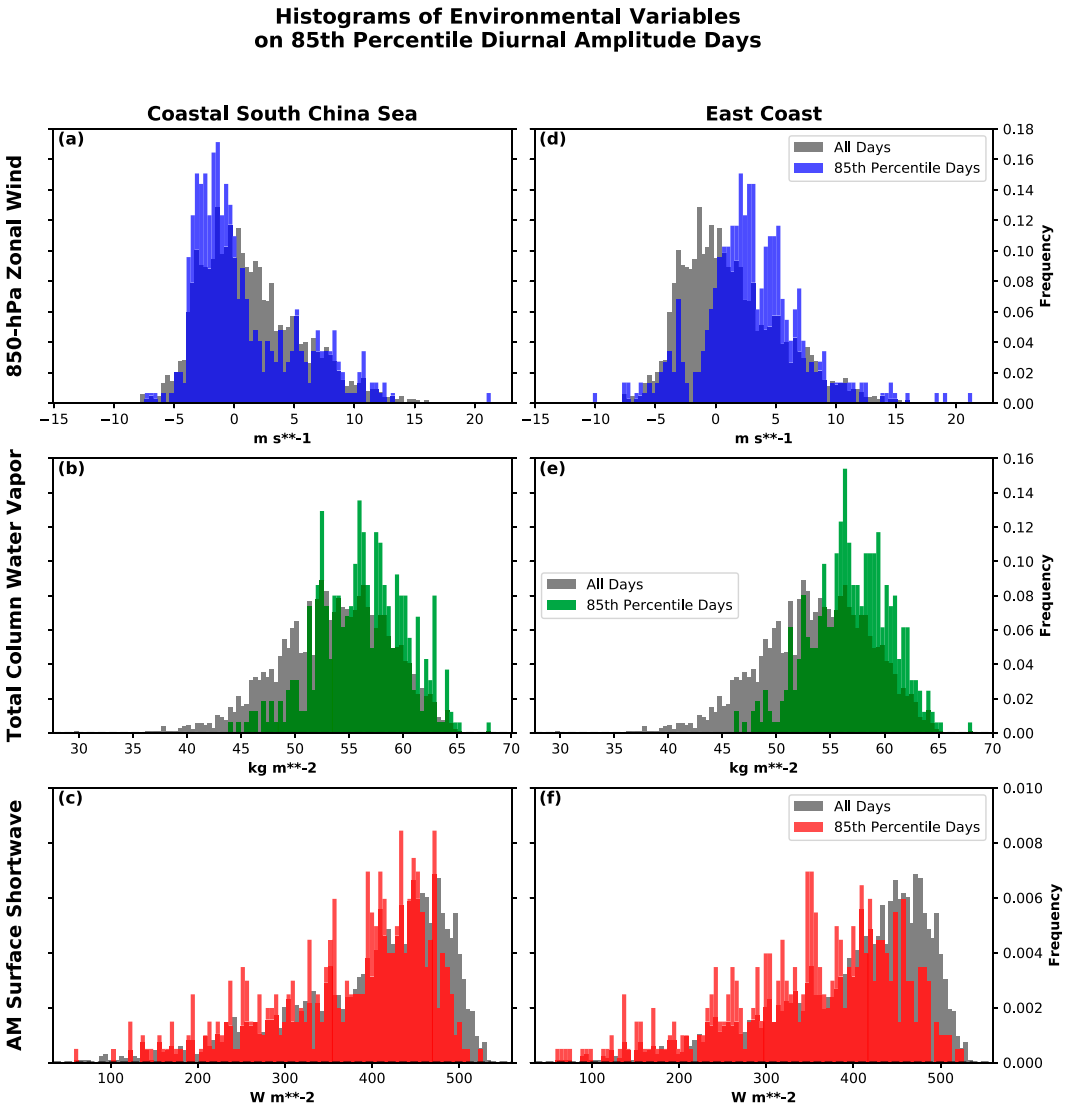

FIG. 6. In gray, histograms of the daily spatial average value inside boxes A–F (Fig. 1) of ERA5 (top) 850-hPa zonal wind (m s^{-1}), (middle) total column water vapor (kg m^{-2}), and (bottom) 0600–1200 LT mean surface shortwave radiation (W m^{-2}). The histogram in color is the histogram of the same variables, but only for days in which the diurnal cycle amplitude exceeded its 85th percentile over (a)–(c) the coastal South China Sea (box B in Fig. 1) and (d)–(f) the east coast of Luzon (box E in Fig. 1). Binned ERA5 variables still come from boxes A–F together, but the diurnal cycle inside each sub-box determines the days from which to derive the distribution. There are 420 DCA85 days for each subregion.

near zero to easterly winds. However, there are positive anomalies in the upper-right quadrant (e.g., moist, westerly) of the South China Sea offshore box (Fig. 7a), while the strongest anomalies for the west coast land box (Fig. 7c) are generally close to average TCWV, but clearly in easterly u850. This indicates that there may be a slightly stronger sensitivity of the offshore diurnal cycle to moisture over wind, while the land-based diurnal cycle may be slightly more sensitive to wind over moisture. The 2D histograms with insolation against both u850 and TCWV were also considered but, partially due to the higher correlations between those variables, they do not aid interpretation and were excluded.

Figure 8 shows a similar style of 2D histograms, but with anomalies showing the difference in distribution given a certain BSISO phase. Statistically significant anomalies (white dots) in this figure are calculated via a bootstrap described in section 2, and in Natoli and Maloney (2019). This demonstrates that the wind and humidity conditions favorable for a DCA85 day in Fig. 7 are well mapped by some BSISO phases. In BSISO phase 1, the distribution appears heavily centered on the lower right quadrant, indicating westerly winds and below average moisture. In Fig. 7, it is evident that TCWV/u850 values in this quadrant make a DCA85 day much less likely for all subregions, which supports the results described above

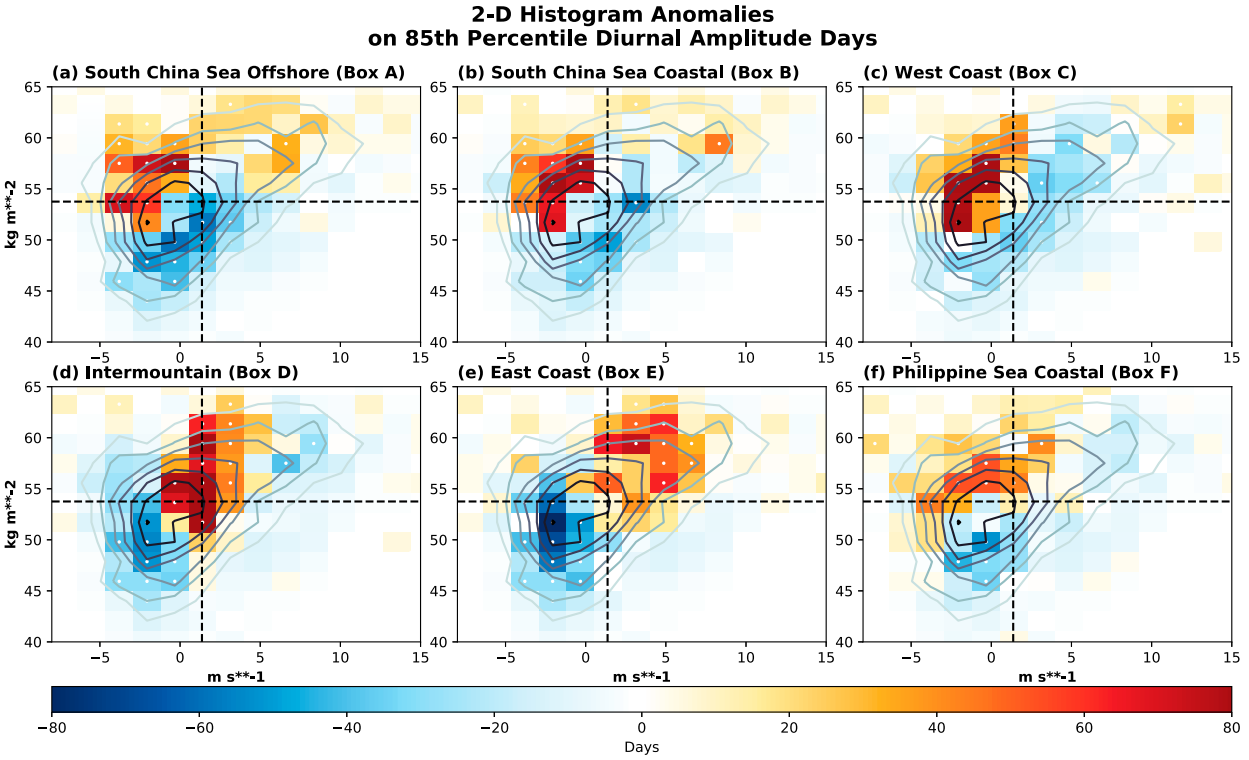

FIG. 7. In contours, the 2D histogram by bins of ERA5 850-hPa zonal wind averaged in boxes A–F together (Fig. 1 on the x axis (m s^{-1}), and ERA5 total column water vapor (kg m^{-2}) averaged in boxes A–F on the y axis, and is the same in each panel. There are 20 total bins in both the zonal wind and total column water vapor distributed evenly between their respective maximum and minimum values. Contours are located every 12 days, with the innermost contour indicating 84 days. A total of 2806 total days are used from JJAS 1998 to 2020 in this analysis. 420 DCA85 days are used. Colors indicate the anomalies in the histogram (of values for boxes A–F together) given that an 85th percentile diurnal cycle amplitude day occurred in one of the six boxes A–F, and varies by panel. Values are scaled before calculating anomalies such that they represent the expected number of days in each 2D bin if 2806 85th percentile days were to occur (i.e., the histogram is divided by 0.15, and then the anomaly is calculated). Boxes C–E include mainly land points, while boxes A, B, and F include mainly oceanic points. The vertical dashed black line indicates the JJAS mean 850-hPa zonal wind, while the horizontal dashed line indicates the JJAS mean total column water vapor. Bins with statistically significant (at the 95% confidence level) anomalies are denoted with a white dot.

in Figs. 3 and 5, which indicated suppressed diurnal cycles in BSISO phase 1. In BSISO phases 2 and 3, the probability distribution shifts more toward easterly wind, but remains dry. This situation can favor a strong diurnal cycle on the west coast (Fig. 7c), but not the other subregions. The composite analysis in Fig. 3 shows that these phases are indeed associated with a substantial diurnal cycle centered on the west coast, but it struggles to propagate offshore. In phase 4, the distribution shifts more toward higher moisture values, but remains easterly. This situation is more favorable for offshore propagation on the west side of the island, which is seen in Fig. 3d. In phases 5–6 (Figs. 8e,f), the upper left quadrant is most favored, which is associated with enhanced odds of a DCA85 day particularly in the SCS. Phases 7–8 tend to have above average moisture, but strongly westerly winds, which is unfavorable for the diurnal cycle on the west coast and in the SCS. However, this quadrant is where the most DCA85 days on the east coast are observed (Fig. 7).

To emphasize the variability across different days that have the same BSISO phase, the same composite Hovmöllers from Fig. 3 are displayed in Figs. 9 and 10, but conditionally sampled by the sign of the zonal wind profile. Days that have an active BSISO in one of the eight phases, but also have an anomalously easterly wind as indicated by the first EOF of the vertical profile of Luzon zonal wind [described in Natoli and Maloney (2023)] less than or equal to -0.25σ are shown in Fig. 9. Those with a westerly wind are shown in Fig. 10. The disparities between the two are striking. Regardless of BSISO phase, restricting the composite to easterly wind leads to the emergence of the clear canonical offshore propagating diurnal cycle on the west side of Luzon. When restricted to westerly wind, this signal disappears entirely, from even the phases exhibiting the most prominent tendency for offshore propagation (phases 4–6). The composites in Fig. 3 can then be interpreted as which wind regime is more likely under a certain BSISO phase. For example, easterly winds are much more likely in phases 2–5 (as indicated by the number in parentheses in the title of each panel, which shows the total number of days in each composite). Westerly days make up the bulk of the BSISO composite days in phases 7, 8, and 1,

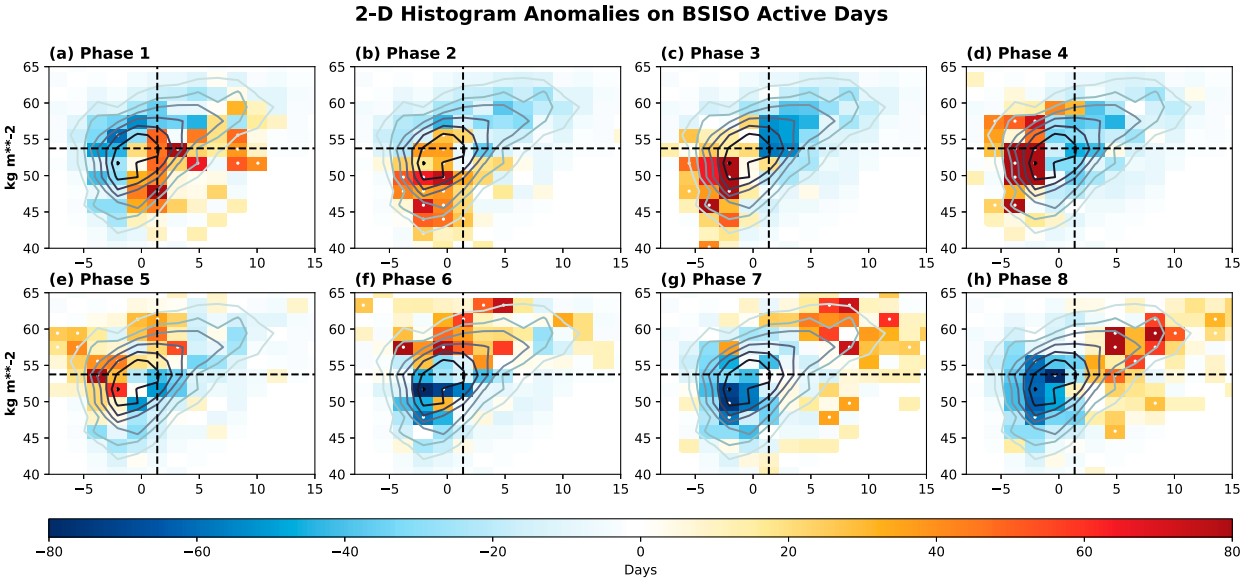

FIG. 8. Contours and vertical lines are as in Fig. 7. Colors indicate the anomalies in the histogram given that the BSISO was active in a certain phase. Values are scaled before calculated anomalies such that they represent the expected number of days in each 2D bin if 2806 days from each BSISO phase were to occur. For example, to display the phase 1 anomaly, the 2D histogram is multiplied by 2806/188 (188 is the number of BSISO phase 1 active days shown in Fig. 2c in JJAS 1998–2020), and then the anomaly is calculated. Values are calculated from boxes A–F together.

while phase 6 is fairly evenly split between the two. Considering the variability within a given phase clearly demonstrates that the BSISO phase simply makes certain environmental conditions more likely, which then impact the local diurnal cycle.

In summary, strong diurnal cycles tend to occur with ambient conditions characterized by near to above average moisture, and weak offshore winds. Since certain BSISO phases make such conditions more probable, the impact of the BSISO on the local diurnal cycle can be understood in terms of its modulation of the local environment, particularly the ambient moisture and low-level wind. The analysis in this section takes a probabilistic approach toward understanding this relationship, and considers the variability within each BSISO phase rather than simply analyzing a composite, which may smooth out much of this variability. The results here support those derived from composite analysis (e.g., Natoli and Maloney 2021, 2023) but are not subject to the same limitations, thus reinforcing the conclusions. Not all BSISO active days in a certain phase are the same, and this analysis shows how the relative probability of a strong diurnal cycle changes given the range of environmental background conditions possible within each phase. The results generally support those found with composite analysis (e.g., Xu and Rutledge 2018; Natoli and Maloney 2019; Chudler et al. 2020; Sakaeda et al. 2020) but broaden the understanding of the variability within the composite, and present a clearer case for the mechanisms involved.

4. CM1 experiments

In this section, idealized model experiments will be discussed in order to control for the mechanisms cited as important for the BSISO-diurnal cycle relationship highlighted in the previous section. The observational analysis provides the best information regarding what is happening in the real atmosphere, but potentially major confounding factors are present. For example, it is challenging to separate the impact of one mechanism from another, which warrants the use of a model to control this more tightly. In the first subsection, we will show that several important aspects of the variability of the local diurnal cycle as a function of BSISO phase can be replicated in the simplified setup here, which validates the use of this setup for sensitivity experiments. The next subsection will explore variations applied to the base state that test sensitivity to specific aspects of the environmental background conditions such as wind and moisture. Throughout the section, only meridionally averaged results are discussed.

a. Control experiments

Hovmöller diagrams of the full 7 days of the control simulations with BSISO phases 3 and 7 base states are shown in Fig. 11. Convection develops over land every afternoon and exhibits some offshore propagation on most days. There is some variability in the strength of precipitation and the extent of offshore propagation, but no clear trends in behavior after the first day. Thus, for much of the next few subsections, a daily composite across the 7 days will be used to ease the interpretation and smooth random variability.

Figure 12 shows the results of this composite for control simulations from all eight BSISO phases. Comparing these results to Fig. 3 reveals several important insights. Starting with the similarities, it is evident that precipitation in the model is diurnally driven, with a peak over land around 1700 that then

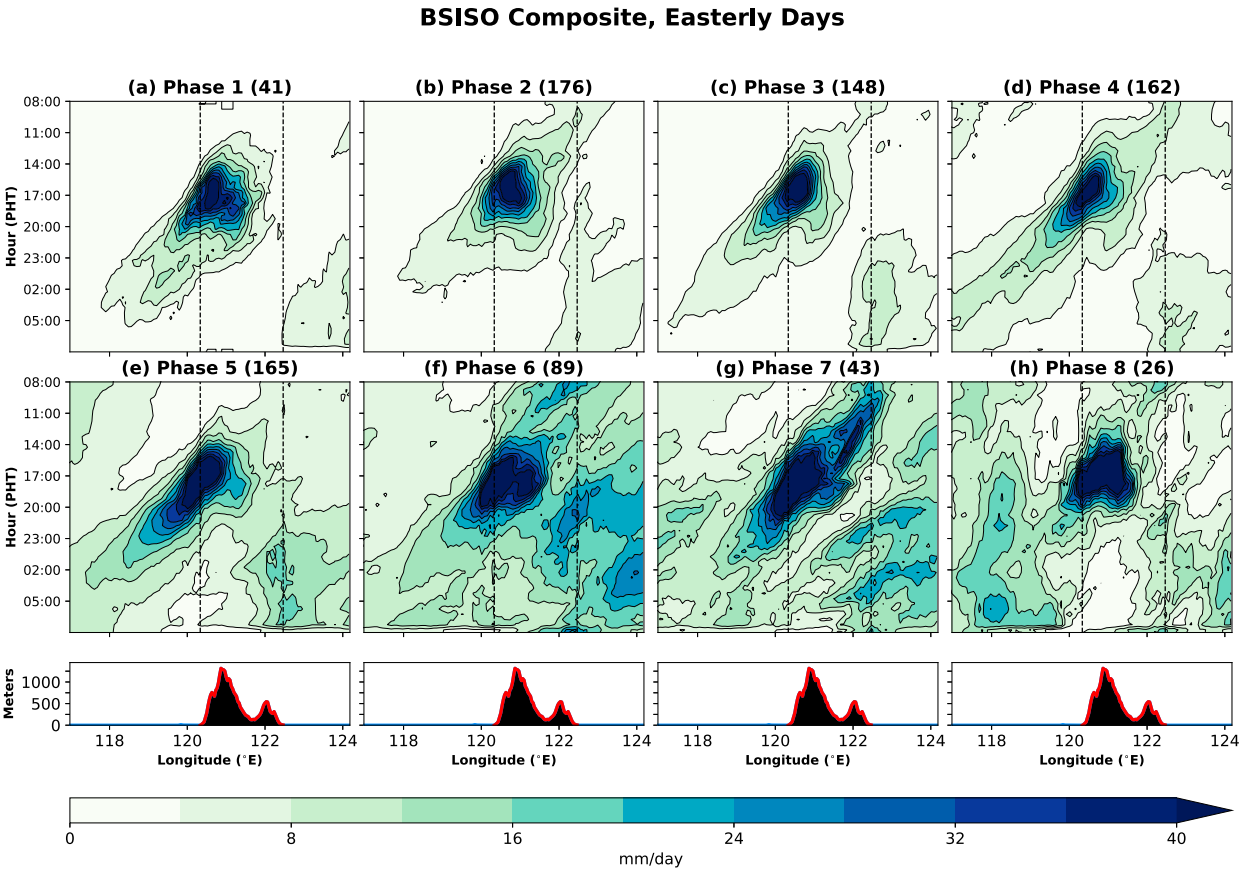

FIG. 9. As in Fig. 3, but with the composite restricted to BSISO active days in a certain phase on which the first EOF of the Luzon vertical profile of zonal wind described in Natoli and Maloney (2023) was less than or equal to -0.25σ, indicating anomalous easterly winds. The number in parentheses next to the title indicates the number of days in each composite.

slowly propagates offshore at around 3–6 m s^{-1}. The phase 3 and 4 base states lead to precipitation clustered closer to the western coast as in observations. In most simulations, a very weak precipitation signal initiates in the early afternoon on both coasts, and propagates inland until the two sea-breeze fronts converge, leading to deep convection and heavier precipitation rates (Saito et al. 2001; Natoli and Maloney 2023). The general preference for a strong diurnal cycle over land in the suppressed BSISO and transition to active BSISO base state is also well replicated. Furthermore, the most obvious offshore propagation occurs with phase 3–6 base states, coinciding with the best propagation into the SCS in observations (Figs. 3e,f). We note that precipitation propagates exclusively eastward with the phase 6 base state rather than both directions but mainly westward in observations (Figs. 3, 9, and 10), but the intensity of offshore precipitation is elevated compared to phases 7, 8, 1, and 2. With the phase 7–8 base states, the diurnal cycle is weaker and shifted to the east side of the island.

There are also several important differences between the model depiction and the real atmosphere. The model completely lacks any nondiurnally driven precipitation. While observations show significant precipitation at all times of day, especially over the coastal SCS during the BSISO active state, the model is unable to reproduce this. The only oceanic precipitation produced is that which is clearly associated with offshore propagation of convection that initiated over land in the afternoon. This is not necessarily a weakness though, as it allows the claim to be made that most precipitation is due to the diurnal cycle in this simulation, and thus removes one confounding variable in the real atmosphere of determining how much precipitation is related to the diurnal cycle. Propagation also only occurs in one direction in a specific phase, but both westward and eastward propagation have generally similar propagation speeds and precipitation intensity (Fig. 12). In the observations, westward propagation is clearly dominant over eastward, but there is some evidence of propagation occurring in both directions in a single phase (Figs. 3, 9, and 10). In the real composites, a range of different days with varying conditions were present, while the composite base state used in the model only provides one of many possible realizations.

Based on the aspects that the model captures well, the successive sensitivity experiments aim to test the sensitivity of the tropical diurnal cycle behavior to the environmental background conditions. We aim to determine which aspects of the ambient atmosphere determine why a strong diurnal cycle

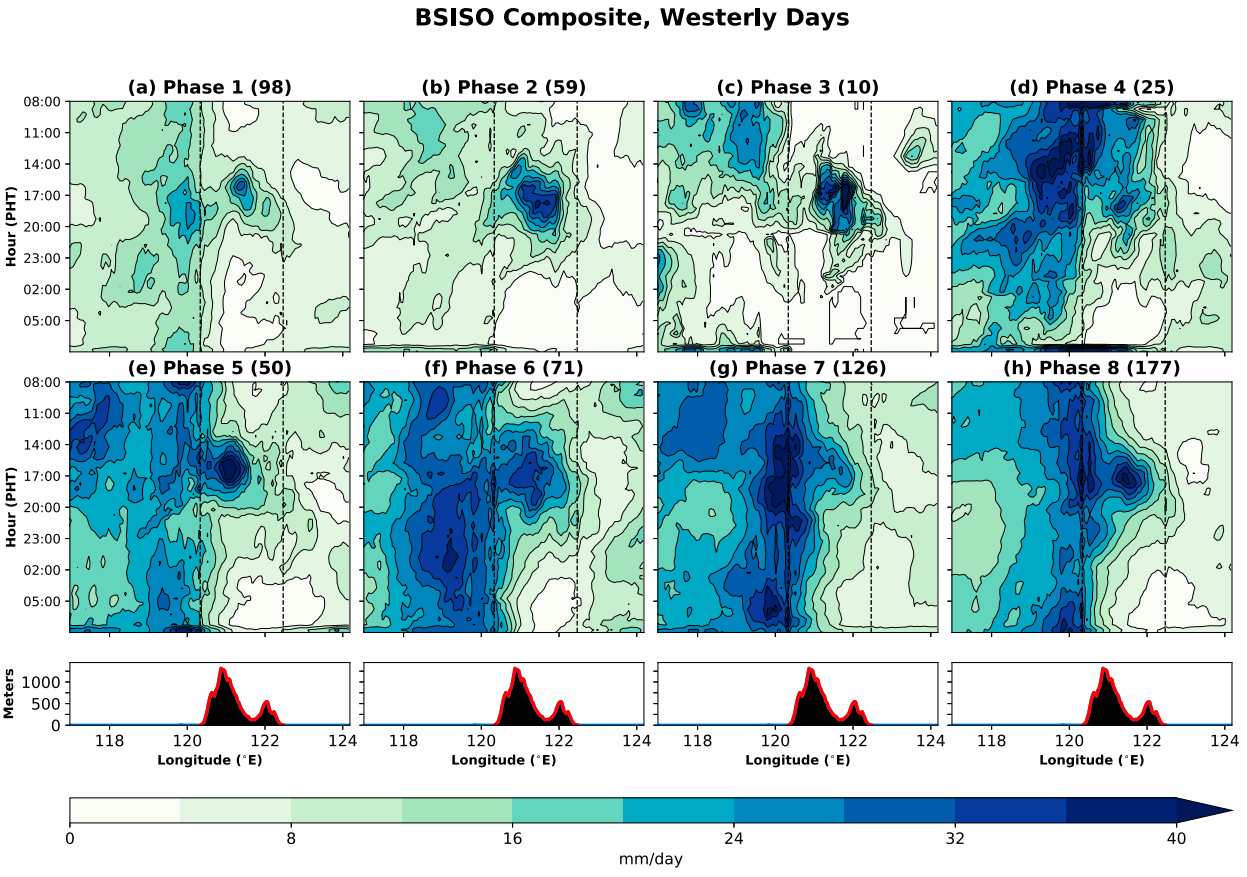

FIG. 10. As in Fig. 3, but with the composite restricted to BSISO active days in a certain phase on which the first EOF of the Luzon vertical profile of zonal wind described in Natoli and Maloney (2023) was greater than or equal to $+0.25\sigma$, indicating anomalous westerly winds. The number in parentheses next to the title indicates the number of days in each composite.

occurs over land during phases 2–5, why the opposite is apparent in phases 7, 8, and 1, how much precipitation will be produced by offshore-propagating convection, and which direction convection will propagate.

b. Base state sensitivity experiments

1) WIND

Next, the BSISO Wind Only experiments will be discussed. In this set, we only vary the base-state zonal wind profile across simulations, while all other variables have a base state fixed at the JJAS mean. Figure 13 shows the composite diurnal cycles for the Wind Only experiments. At first glance, these results look very similar to the control. By only changing the base-state wind profile, several qualitative aspects of the diurnal cycle behavior are retained—notably, the strong land-based diurnal cycles in phases 2–5, the weak diurnal cycle on the eastern coast in phases 7, 8, and 1, and the significant offshore propagation in phases 3–6. This supports the argument that the BSISO modulation of the wind profiles is one of the primary mechanisms through which it impacts the diurnal cycle (Short et al. 2019; Peatman et al. 2021; Natoli and Maloney 2023). Critically, the strong onshore wind appears to be the primary variable responsible for the reduction in diurnal cycle strength during the BSISO active state (phases 6–8). The model produces a stronger diurnal cycle on the leeward side of the island under a weak to moderate background wind, similar to previous modeling studies and observations (Ho et al. 2008; Virts et al. 2013; Liang et al. 2017; Wang and Sobel 2017; Qian 2020). Conversely, a strong wind, particularly in the lower atmosphere, reduces the magnitude of diurnally generated precipitation (Fig. 7) by limiting the land–sea contrast, and thus the sea-breeze circulation (Shige et al. 2017; Wu et al. 2017; Yokoi et al. 2019).

Since the differences compared to the control runs are difficult to discern in Fig. 13, Fig.14 shows the average precipitation rate over land, and over ocean on the leeward side of the island for both the Control and Wind Only simulations. Precipitation variability in the control simulations appears to be regulated by more than wind variability alone. Over both land and water, phases 1–4 produce more precipitation when only the BSISO wind is used, whereas phases 5–8 produce less. Not coincidentally, phases 1–4 have drier than average moisture profiles in BSISO composites, while phases 5–8 are more moist (Fig. 2b). The reduced ambient moisture during the suppressed BSISO phases inhibits what would be a stronger

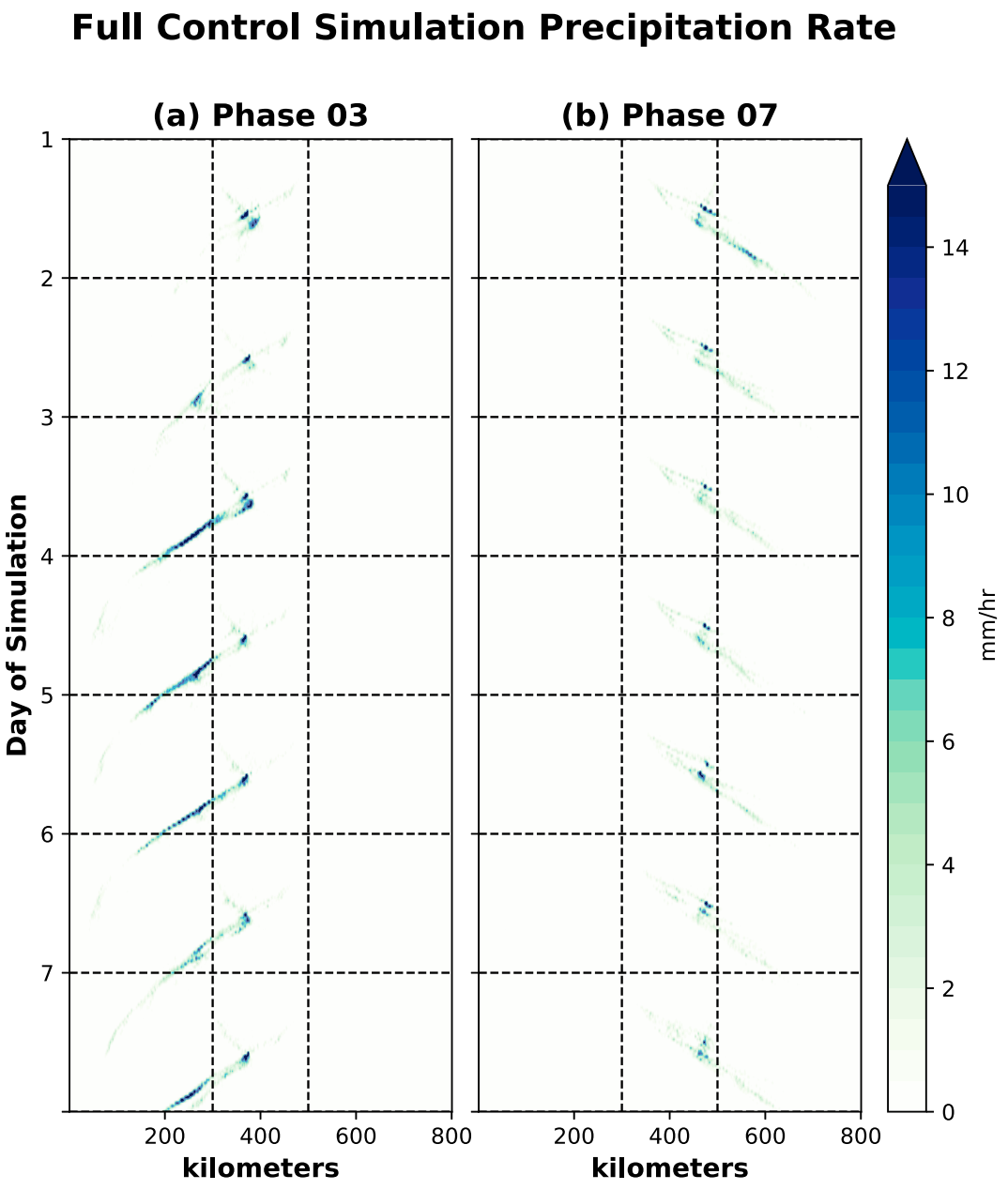

FIG. 11. Meridionally averaged precipitation rate (mm h^{-1}) for the full 7-day simulation the Cloud Model 1 (CM1) control simulations with (a) a BSISO phase 3 base state and (b) a BSISO phase 7 base state. The x axis in each is in kilometers, with the coastlines marked as vertical dashed black lines. The time 0500 LT on each day is noted as a horizontal dashed black line.

diurnal cycle based on weak to moderate easterlies alone, hence reflected in an increase in precipitation during phases 1–4 when only the wind is varied. The leeward waters see the most precipitation with BSISO phase 3–4 winds, but once the rest of the environmental profile is factored in as in the control, the most precipitation occurs with a BSISO phase 5–6 profile. This result is unsurprising and is consistent with the observational results discussed above and in the literature, highlighting the tight relationship between free-tropospheric moisture and precipitation in the tropics (Bretherton et al. 2004; Hassim et al. 2016; Vincent and Lane 2017, 2018; Lu et al. 2019; Sakaeda et al. 2020). The relationship between moisture and precipitation in CM1 will be explored in more detail next.

2) MOISTURE

The next set of experiments takes a closer look at the role of ambient moisture by exploring a wider range of moisture

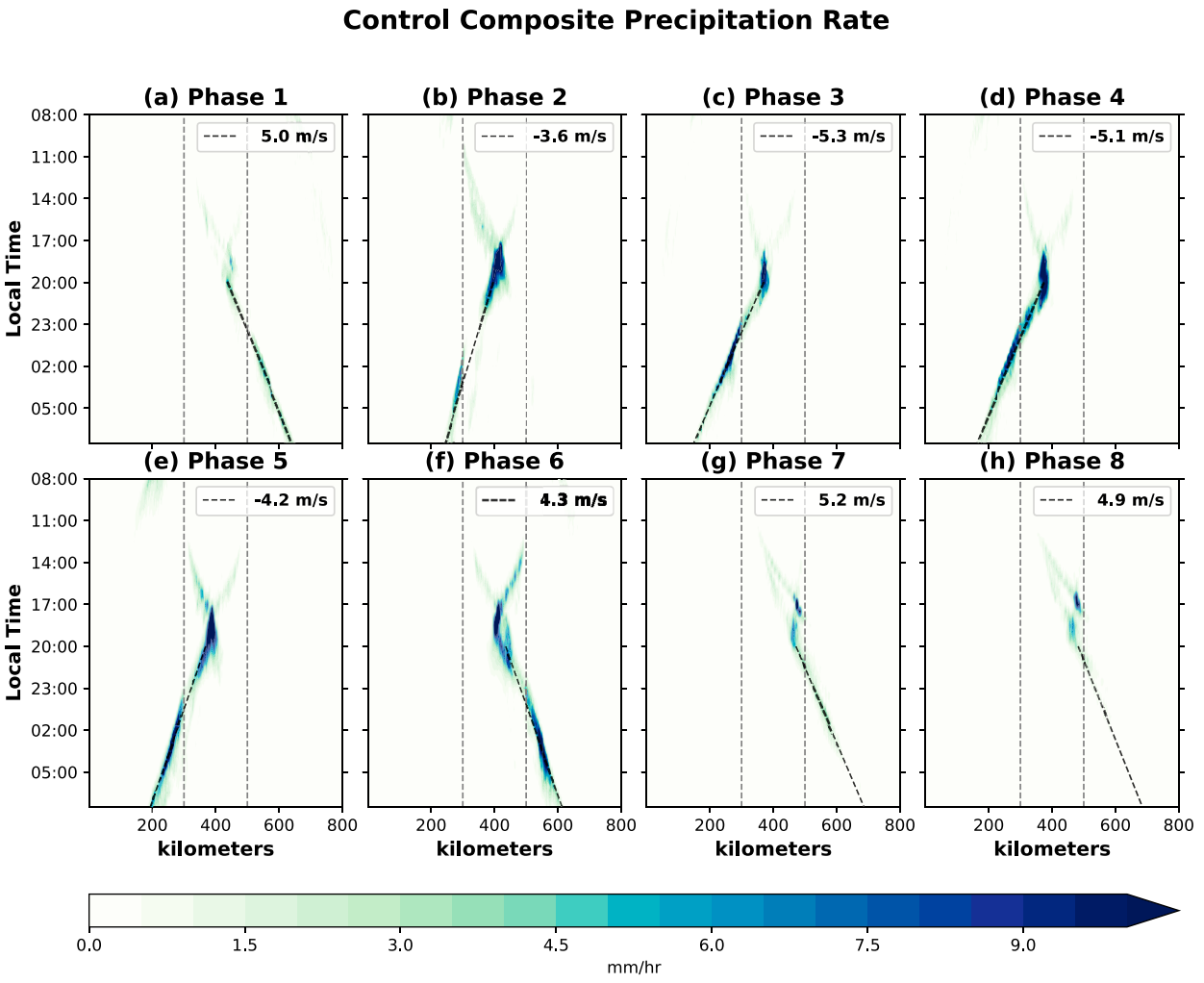

FIG. 12. Daily composite of the 7-day control CM1 simulations showing meridionally averaged precipitation rate (mm h^{-1}) by longitude at 1-km resolution. Each simulation varies the base state with ERA5 BSISO composite profiles. The wind and moisture profiles are shown in Figs. 2a and 2b. Dashed gray lines note the coastlines, and the dashed black line follows a line of best fit connecting the longitude of maximum precipitation rate at each time between 2000 and 0800 LT. This is calculated based on precipitation rate smoothed to 5-km resolution.

profiles, the details of which are described in section 2. Average precipitation rate by time of day in the diurnal composite for each simulation is shown in Fig. 15. Figures 15a and 15c show the precipitation rate averaged over the modeled landmass (300–500-km), while Figs. 15b and 15d are averaged over ocean grid points on the leeward side of the landmass (0–300 km in easterly flow, 500–800 km in westerly flow). The expected result of increasing precipitation with increasing moisture emerges with both BSISO phases 3 and 7 winds. Differences between the wettest and the driest experiment are dramatic, likely resulting from the fairly extreme moisture profiles used here. Interestingly, the diurnal cycle over land does appear to peak earlier in the day under high moisture conditions, consistent with Riley Dellaripa et al. (2020), who showed an earlier diurnal cycle peak during BSISO active conditions when topography was removed from the model. Significantly more rainfall in the higher moisture experiments again emphasizes the importance of having sufficient ambient water vapor content to attain significant precipitation in the tropics (Holloway and Neelin 2009, 2010), since convection developing in a dry environment will entrain dry air and weaken (Kuo et al. 2017).

While the following paragraph is not critical to the main goals of this study, the results are interesting enough to warrant some speculative discussion for readers interested in the finer details of the model behavior. Examination of precipitation in the offshore environment (Figs. 15b,d) by moisture experiment reveals surprising results. With BSISO phase 3 winds, there appears to be little to no relationship between the ambient moisture and offshore precipitation. The lowest (but broadest) peak in precipitation rate occurs with the $+1.5\sigma$ moisture, while the highest precipitation rate occurs with phase 3 moisture, which is the second driest sounding studied. The expected result would be for the offshore precipitation to be even more

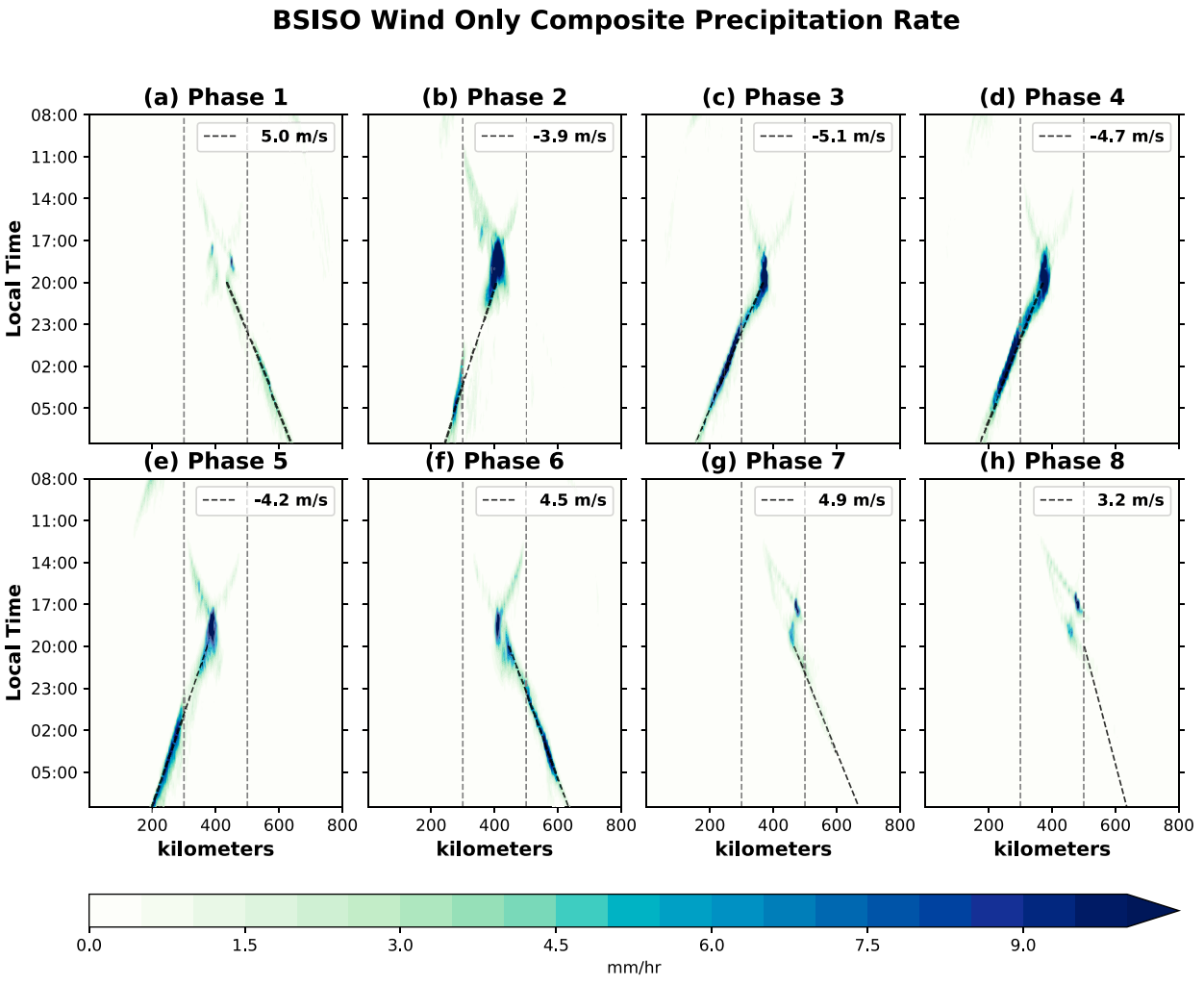

FIG. 13. As in Fig. 12, but for the wind-only CM1 simulations. The base state for these simulations uses the wind profile from each BSISO phase composite (shown in Fig. 2a), and the JJAS mean profile for the moisture and thermodynamic variables.

stratified by moisture than land-based precipitation based on the results from section 3. We present some possible explanations for this discrepancy, but will leave a more conclusive answer to future work. First, the phase 3 wind profile is easterly throughout the column, and thus moisture advection by the mean wind acts to moisten the environment west of the island. The offshore environment on the leeward side of the island moistens over the first two days of the simulation (Fig. S1 in the online supplemental material) and results in about a 10% increase in TCWV by day 3, while the east side of the island exhibits a 10% decrease. The large-scale nudging techniques employed to maintain the base state only nudge the domain mean, so a redistribution of moisture across the domain will not be corrected. Thus, the driest simulations are not quite as dry in the offshore environment as they should be had the initial profile stayed uniform. However, this does not explain the relative lack of offshore precipitation in the $+1.5\sigma$ experiment, which necessitates speculating on another possible mechanism. This simulation results in a much stronger cold pool that develops earlier in the day (Fig. S2) due to the early peak over land (Fig. 15a). Deep convection initiates along the leeward coast's inland propagating sea-breeze front in both $+1.5\sigma$ experiments *before* the opposing sea-breeze fronts converge, and continues to propagate inland after the fronts converge (Fig. S3). This is unlike each of the control simulations, in which the onset of deep convection occurs *after* the sea-breeze fronts converge. As a result, instability may be more depleted on the leeward side of the island due to the earlier convective onset. A time series of convective available potential energy (CAPE; Fig. S4) indeed indicates that the $+1.5\sigma$ moisture experiment actually has the *lowest* CAPE on the west side of the island compared to all three other moisture experiments with BSISO phase 3 winds. Another possible explanation is that in the dry state, convection develops along a very narrow density current front, the only location in which there is sufficient lift to attain deep convection. The higher moisture environment is not as confined to the density current boundary, resulting in a broader precipitation peak.

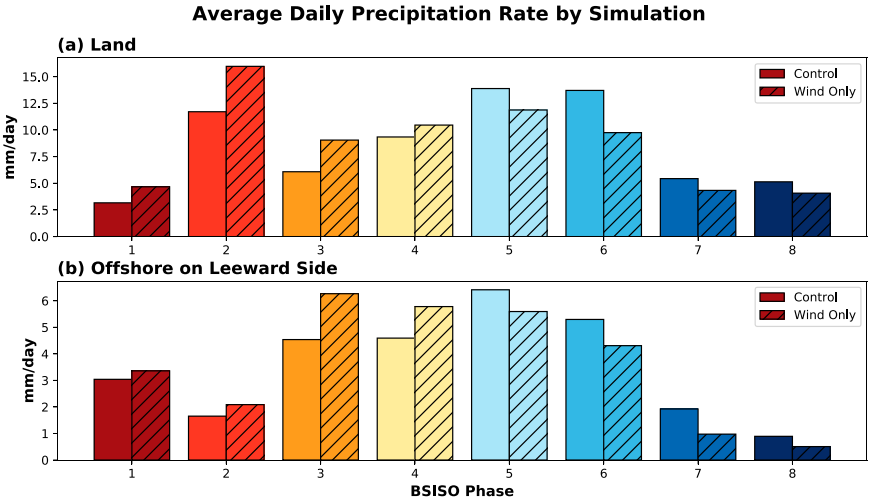

FIG. 14. (a) CM1 precipitation rate (mm day^{-1}) averaged over land for each of simulations with varying BSISO composite derived base states. Bars for the control simulations (Fig. 12) are solid colors, while those for the wind-only simulations (Fig. 13) are hatched. (b) As in (a), but averaged over the ocean grid points on the leeward side of the island (west for phases 2–5; east for others).

Overall, the results of the wind and moisture experiments support the conclusions derived from section 3, in that the BSISO modulation of ambient wind and moisture is what affects the local diurnal cycle. We can replicate several aspects of the BSISO–diurnal cycle relationship in an idealized model with only the base state from a composite BSISO profile, although the response to variable moisture profiles over the ocean in CM1 is more nuanced than expected.

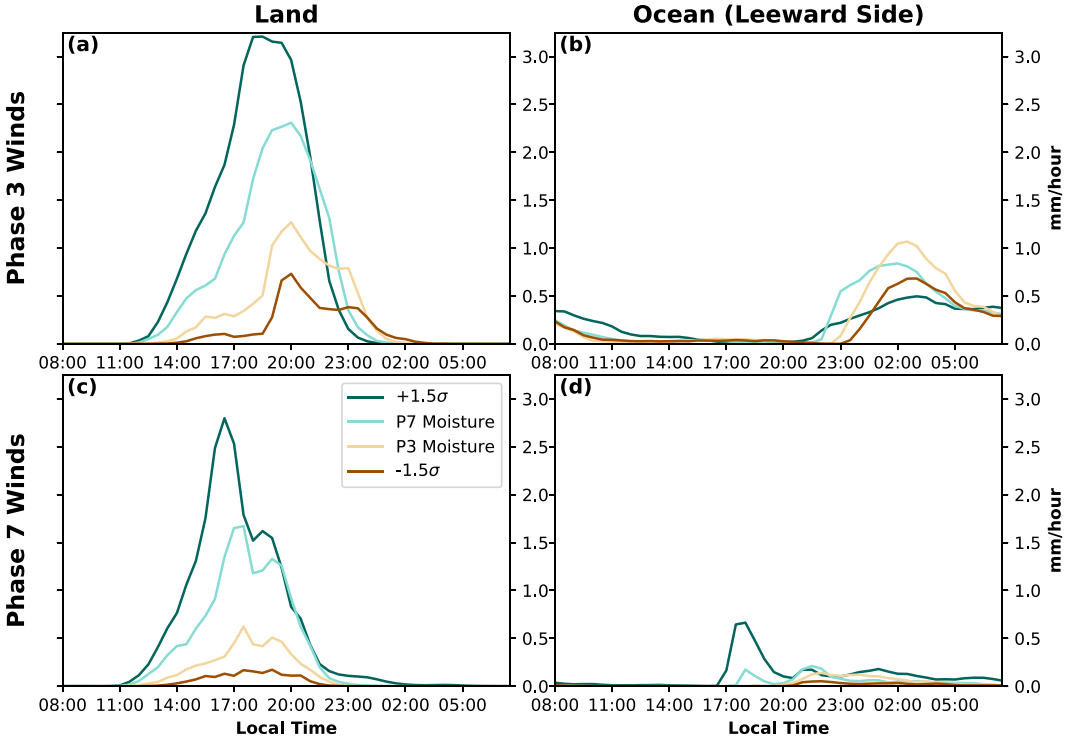

FIG. 15. Composite precipitation rate (mm h^{-1}) for the moisture experiments averaged (left) over land and (right) over ocean on the leeward side of the island. In simulations (a),(b) the BSISO phase 3 wind profile is used in the base state and (c),(d) the BSISO phase 7 wind profile is forced in the base state.

5. Conclusions

The mechanisms through which large-scale patterns of tropical convective variability such as the MJO/BSISO impact the local diurnal cycle on tropical islands were examined. Specifically, we show which characteristics of the local environment, potentially modulated by the MJO/BSISO, result in substantial changes to diurnal cycle behavior. Using Luzon Island in the northern Philippines as an example, a probabilistic approach to observational analysis was employed in lieu of the conventional composite analysis to examine diurnal cycle variability. Such techniques reveal more about the range of possible environments found within a certain phase of the BSISO, and the relative likelihood of a robust diurnally driven precipitation in varying regimes. This contributes a broader understanding of diurnal cycle behavior than established through the composite analyses of prior research (e.g., Rauniyar and Walsh 2011; Peatman et al. 2014; Birch et al. 2016; Hassim et al. 2016; Vincent and Lane 2016; Sakaeda et al. 2017). Idealized model simulations with CM1 build upon the observational results and allow for the isolation of low-level wind and ambient moisture, highlighted by prior research as potentially important environmental variables for understanding the mechanisms of the BSISO–diurnal cycle relationship (e.g., Birch et al. 2016; Vincent and Lane 2017; Natoli and Maloney 2019, 2021; Short et al. 2019; Sakaeda et al. 2020). The results address the nature of the diurnal cycle, its offshore propagation, and the physical mechanisms regulating its relationship to large-scale modes of variability (Virts et al. 2013; Wang and Sobel 2017; Yokoi et al. 2019; Qian 2020; Peatman et al. 2021). While we have used Luzon Island during boreal summer as a case study, it may be possible to generalize our results to the boreal winter MJO and other islands in the MC. A similar analysis focusing on the more widely studied boreal winter MJO in the Indonesian MC could prove insightful in the future. The main findings of this research are summarized as follows:

- The probability of a high-amplitude diurnal cycle over the west coast of Luzon is maximized in observations during the suppressed BSISO phases and the transition to active (Figs. 3c–e and 5c). In the coastal South China Sea (SCS) offshore propagation is maximized in the phases covering the transition from suppressed to active. (Figs. 3e,f and 5a,b).
- High-amplitude observed diurnal cycle days tend to occur with weak to moderate offshore low-level wind and near to above average column moisture (Figs. 6a,b,d,e and 7). There appears to be little association with morning insolation (Figs. 6c,f).
- The transition from BSISO suppressed to active conditions (roughly phases 3–6) is most likely to produce the wind and moisture conditions favorable for a high-amplitude diurnal cycle in observations with substantial offshore propagation into the SCS (Figs. 7 and 8).
- Idealized CM1 simulations using a base state derived from BSISO composite wind, moisture, and thermodynamic profiles (Fig. 2) can replicate several important features of the observed diurnal cycle (Fig. 3), including the strong land-based diurnal cycle in the BSISO suppressed and transition phases, strong offshore propagation in the transition phases, and the suppressed diurnal cycle during BSISO active conditions (Figs. 11, 12, and 14).
- Driving the simulations with only the BSISO wind profile and JJAS mean moisture and temperature profiles results in very similar diurnal cycle behavior to the control simulations, emphasizing the importance of the wind profile in producing the observed diurnal cycle modulation by BSISO phase (Figs. 13 and 14). Weak offshore prevailing wind favors an active diurnal cycle with offshore propagation.
- Land-based precipitation exhibits strong sensitivity to ambient moisture in CM1 (Figs. 14 and 15a,c). Moisture anomalies enhance diurnal precipitation during the BSISO active phase, and weaken diurnal precipitation during the suppressed phase, but wind explains the specific preference for strong diurnal cycles during the transition period.

CM1 was able to realistically simulate many well-studied (e.g., Peatman et al. 2014; Sakaeda et al. 2017; Xu and Rutledge 2018; Lu et al. 2019; Natoli and Maloney 2019; Chudler et al. 2020) aspects of the ISO–diurnal cycle relationship with only the BSISO composite profile used in the base state. This strongly suggests that the physical mechanisms regulating this relationship can be reduced to the large-scale modulation of local environmental variables, particularly moisture and wind. We do note that our model setup does have some caveats, the importance of which should be addressed in future research to determine the general applicability of these results to the real atmosphere. For example, our large-scale nudging technique that is required to maintain the base state through a longer simulation does not prevent persistent spatial inhomogeneities from developing within the domain. The model also produces very little oceanic precipitation that is not associated with offshore propagation, and the abundant precipitation in the SCS is an important characteristic of the BSISO active state. Thus, exploring these differences in more detail, including with a different model would be advantageous in order to better understand the deficiencies and unique characteristics of CM1 that may affect our conclusions.

These results also yield several new questions providing avenues for future research. In the real atmosphere, it is possible that the presence of topography and the induced circulations thereof could act as an additional source of low-level convergence that is important for initiating offshore propagation. Thus, the inclusion of topography in our model could prove insightful and build on other research exploring the role of mountains to the diurnal cycle in tropical islands (Riley Dellaripa et al. 2020; Ruppert et al. 2020). Additional sensitivity tests exploring the importance of the width of the island to diurnal cycle behavior could also be insightful. We also plan to test the role of insolation in this model. For example, a constant insolation experiment (i.e., no diurnal cycle) to see if offshore propagation and a natural time scale for convection over land develops in the absence of diurnal forcing. Additional tests could attempt to isolate the BSISO cloud cover variability and its impact on the local diurnal cycle.

Analyzing the importance of the internal cold pool dynamics of deep convection in this model may also be insightful. Exploring these results in the context of extreme precipitation events (e.g., Ferrett et al. 2019) could have broader societal benefits. These proposed paths for future research may provide further clarity regarding the tropical island diurnal cycle and its offshore propagation.

Acknowledgments. This work forms part of the Ph.D. dissertation of Michael Natoli. The authors thank Professors Michael Bell, David Randall, and Jeffrey Niemann for their advice and contributions as committee members. This work was supported by the Office of Naval Research (ONR) under the Propagation of Tropical Intraseasonal Oscillations (PISTON) project N00014-16-1-3087, the NOAA CVP program under Grant NA22OAR4310609, NASA CYGNSS grant 80NSSC21K1004, and the Climate and Large Scale Dynamics Program of the National Science Foundation under Grant AGS-2217785. The authors thank Prof. Susan van den Heever, Dr. Leah Grant, and Prof. Russ Schumacher at Colorado State University for their helpful advice and guidance in designing and running the model experiments.

Data availability statement. CMORPH bias-corrected precipitation data as described in Xie et al. (2017) can be downloaded at https://www.ncei.noaa.gov/data/cmorph-high-resolution-global-precipitation-estimates/access/30min/8km/. ERA5 data as described in Hersbach et al. (2020) can be downloaded at https://www.ecmwf.int/en/forecasts/datasets/reanalysis-datasets/era5. The code for CM1 can be downloaded from https://www2.mmm.ucar.edu/people/bryan/cm1/. Output from the simulations described in this study will be made available upon request to the authors.

REFERENCES

Annamalai, H., and J. M. Slingo, 2001: Active/break cycles: Diagnosis of the intraseasonal variability of the Asian summer monsoon. *Climate Dyn.*, **18**, 85–102, https://doi.org/10.1007/s003820100161.

Bergemann, M., C. Jakob, and T. P. Lane, 2015: Global detection and analysis of coastline-associated rainfall using an objective pattern recognition technique. *J. Climate*, **28**, 7225–7236, https://doi.org/10.1175/JCLI-D-15-0098.1.

Biasutti, M., S. E. Yuter, C. D. Burleyson, and A. H. Sobel, 2012: Very high resolution rainfall patterns measured by TRMM Precipitation Radar: Seasonal and diurnal cycles. *Climate Dyn.*, **39**, 239–258, https://doi.org/10.1007/s00382-011-1146-6.

Birch, C. E., S. Webster, S. C. Peatman, D. J. Parker, A. J. Matthews, Y. Li, and M. E. E. Hassim, 2016: Scale interactions between the MJO and the western Maritime Continent. *J. Climate*, **29**, 2471–2492, https://doi.org/10.1175/JCLI-D-15-0557.1.

Bretherton, C. S., M. E. Peters, and L. E. Back, 2004: Relationships between water vapor path and precipitation over the tropical oceans. *J. Climate*, **17**, 1517–1528, https://doi.org/10.1175/1520-0442(2004)017<1517:RBWVPA>2.0.CO;2.

Bryan, G. H., and J. M. Fritsch, 2002: A benchmark simulation for moist nonhydrostatic numerical models. *Mon. Wea. Rev.*, **130**, 2917–2928, https://doi.org/10.1175/1520-0493(2002)130<2917:ABSFMN>2.0.CO;2.

——, and H. Morrison, 2012: Sensitivity of a simulated squall line to horizontal resolution and parameterization of microphysics. *Mon. Wea. Rev.*, **140**, 202–225, https://doi.org/10.1175/MWR-D-11-00046.1.

C3S, 2017: ERA5: Fifth generation of ECMWF atmospheric reanalyses of the global climate. CDS, accessed 16 February 2021, https://cds.climate.copernicus.eu/cdsapp#!/home.

Chen, T.-C., and J.-M. Chen, 1995: An observational study of the South China Sea monsoon during the 1979 summer: Onset and life cycle. *Mon. Wea. Rev.*, **123**, 2295–2318, https://doi.org/10.1175/1520-0493(1995)123<2295:AOSOTS>2.0.CO;2.

——, and K. Takahashi, 1995: Diurnal variation of outgoing longwave radiation in the vicinity of the South China Sea: Effect of intraseasonal oscillation. *Mon. Wea. Rev.*, **123**, 566–577, https://doi.org/10.1175/1520-0493(1995)123<0566:DVOOLR>2.0.CO;2.

Chen, X., F. Zhang, and J. H. Ruppert Jr., 2019: Modulations of the diurnal cycle of coastal rainfall over South China caused by the boreal summer intraseasonal oscillation. *J. Climate*, **32**, 2089–2108, https://doi.org/10.1175/JCLI-D-18-0786.1.

Chudler, K., W. Xu, and S. A. Rutledge, 2020: Impact of the boreal summer intraseasonal oscillation on the diurnal cycle of precipitation near and over the island of Luzon. *Mon. Wea. Rev.*, **148**, 1805–1827, https://doi.org/10.1175/MWR-D-19-0252.1.

DeMott, C. A., C. Stand, and D. A. Randall, 2013: Northward propagation mechanisms of the boreal summer intraseasonal oscillation in the ERA-Interim and SP-CCSM. *J. Climate*, **26**, 1973–1992, https://doi.org/10.1175/JCLI-D-12-00191.1.

Ferrett, S., G.-Y. Yang, S. J. Woolnough, J. Methven, K. Hodges, and C. E. Holloway, 2019: Linking extreme precipitation in Southeast Asia to equatorial waves. *Quart. J. Roy. Meteor. Soc.*, **146**, 665–684, https://doi.org/10.1002/qj.3699.

Gill, A. E., 1980: Some simple solutions for heat-induced tropical circulation. *Quart. J. Roy. Meteor. Soc.*, **106**, 447–462, https://doi.org/10.1002/qj.49710644905.

Hassim, M. E. E., T. P. Lane, and W. W. Grabowski, 2016: The diurnal cycle of rainfall over New Guinea in convection-permitting WRF simulations. *Atmos. Chem. Phys.*, **16**, 161–175, https://doi.org/10.5194/acp-16-161-2016.

Hersbach, H., and Coauthors, 2020: The ERA5 global reanalysis. *Quart. J. Roy. Meteor. Soc.*, **146**, 1999–2049, https://doi.org/10.1002/qj.3803.

Ho, C.-H., M.-S. Park, Y.-S. Choi, and Y. N. Takayabu, 2008: Relationship between intraseasonal oscillation and diurnal variation of summer rainfall over the South China Sea. *Geophys. Res. Lett.*, **35**, L03701, https://doi.org/10.1029/2007GL031962.

Holloway, C. E., and J. D. Neelin, 2009: Moisture vertical structure, column water vapor, and tropical deep convection. *J. Atmos. Sci.*, **66**, 1665–1683, https://doi.org/10.1175/2008JAS2806.1.

——, and ——, 2010: Temporal relations of column water vapor and tropical precipitation. *J. Atmos. Sci.*, **67**, 1091–1105, https://doi.org/10.1175/2009JAS3284.1.

Hong, S.-Y., Y. Noh, and J. Dudhia, 2006: A new vertical diffusion package with an explicit treatment of entrainment processes. *Mon. Wea. Rev.*, **134**, 2318–2341, https://doi.org/10.1175/MWR3199.1.

Houze, R. A., Jr., S. G. Geotis, F. D. Marks Jr., and A. K. West, 1981: Winter monsoon convection in the vicinity of North Borneo. Part I: Structure and time variation of the clouds and precipitation. *Mon. Wea. Rev.*, **109**, 1595–1614, https://doi.org/10.1175/1520-0493(1981)109<1595:WMCITV>2.0.CO;2.

Jiang, X., Á. F. Adames, M. Zhao, D. Waliser, and E. Maloney, 2018: A unified moisture mode framework for seasonality of

the Madden–Julian oscillation. *J. Climate*, **31**, 4215–4224, https://doi.org/10.1175/JCLI-D-17-0671.1.

Jiménez, P. A., J. Dudhia, J. F. González-Ruoco, J. Navarro, J. P. Montávez, and E. García-Bustamante, 2012: A revised scheme for the WRF surface layer formulation. *Mon. Wea. Rev.*, **140**, 898–918, https://doi.org/10.1175/MWR-D-11-00056.1.

Joyce, R. J., J. E. Janowiak, P. A. Arkin, and P. Xie, 2004: CMORPH: A method that produces global precipitation estimates from passive microwave and infrared data at high spatial and temporal resolution. *J. Hydrometeor.*, **5**, 487–503, https://doi.org/10.1175/1525-7541(2004)005<0487:CAMTPG>2.0.CO;2.

Kikuchi, K., B. Wang, and Y. Kajikawa, 2012: Bimodal representation of the tropical intraseasonal oscillation. *Climate Dyn.*, **38**, 1989–2000, https://doi.org/10.1007/s00382-011-1159-1.

Kilpatrick, T., S.-P. Xie, and T. Nasuno, 2017: Diurnal convection–wind coupling in the Bay of Bengal. *J. Geophys. Res. Atmos.*, **122**, 9705–9720, https://doi.org/10.1002/2017JD027271.

Kuo, Y.-H., J. D. Neelin, and C. R. Mechoso, 2017: Tropical convection transition statistics and causality in the water vapor–precipitation relation. *J. Atmos. Sci.*, **74**, 915–931, https://doi.org/10.1175/JAS-D-16-0182.1.

Lau, K.-M., and P. H. Chan, 1986: Aspects of the 40–50 day oscillation during the northern summer as inferred from outgoing longwave radiation. *Mon. Wea. Rev.*, **114**, 1354–1367, https://doi.org/10.1175/1520-0493(1986)114<1354:AOTDOD>2.0.CO;2.

Lawrence, D. M., and P. J. Webster, 2002: The boreal summer intraseasonal oscillation: Relationship between northward and eastward movement of convection. *J. Atmos. Sci.*, **59**, 1593–1606, https://doi.org/10.1175/1520-0469(2002)059<1593:TBSIOR>2.0.CO;2.

Lee, J.-Y., B. Wang, M. C. Wheeler, X. Fu, D. E. Waliser, and I.-S. Kang, 2013: Real-time multivariate indices for the boreal summer intraseasonal oscillation over the Asian summer monsoon region. *Climate Dyn.*, **40**, 493–509, https://doi.org/10.1007/s00382-012-1544-4.

Liang, Z., D. Wang, Y. Liu, and Q. Cai, 2017: A numerical study of the convection triggering and propagation associated with sea breeze circulation over Hainan Island. *J. Geophys. Res. Atmos.*, **122**, 8567–8592, https://doi.org/10.1002/2016JD025915.

Lu, J., T. Li, and L. Wang, 2019: Precipitation diurnal cycle over the Maritime Continent modulated by the MJO. *Climate Dyn.*, **53**, 6489–6501, https://doi.org/10.1007/s00382-019-04941-8.

Madden, R. A., and P. R. Julian, 1971: Detection of a 40–50 day oscillation in the zonal wind in the tropical Pacific. *J. Atmos. Sci.*, **28**, 702–708, https://doi.org/10.1175/1520-0469(1971)028<0702:DOADOI>2.0.CO;2.

——, and ——, 1972: Description of global-scale circulation cells in the tropics with a 40–50 day period. *J. Atmos. Sci.*, **29**, 1109–1123, https://doi.org/10.1175/1520-0469(1972)029<1109:DOGSCC>2.0.CO;2.

——, and ——, 1994: Observations of the 40–50-day tropical oscillation—A review. *Mon. Wea. Rev.*, **122**, 814–837, https://doi.org/10.1175/1520-0493(1994)122<0814:OOTDTO>2.0.CO;2.

Maloney, E. D., and D. L. Hartmann, 1998: Frictional moisture convergence in a composite life cycle of the Madden–Julian oscillation. *J. Climate*, **11**, 2387–2403, https://doi.org/10.1175/1520-0442(1998)011<2387:FMCIAC>2.0.CO;2.

Mapes, B. E., T. T. Warner, M. Xu, and A. J. Negri, 2003: Diurnal patterns of rainfall in northwestern South America. Part I: Observations and context. *Mon. Wea. Rev.*, **131**, 799–812, https://doi.org/10.1175/1520-0493(2003)131<0799:DPORIN>2.0.CO;2.

Mori, S., and Coauthors, 2004: Diurnal land–sea rainfall peak migration over Sumatera Island, Indonesian Maritime Continent, observed by TRMM satellite and intensive rawinsonde soundings. *Mon. Wea. Rev.*, **132**, 2021–2039, https://doi.org/10.1175/1520-0493(2004)132<2021:DLRPMO>2.0.CO;2.

National Geophysical Data Center, 2006: 2-minute Gridded Global Relief Data (ETOPO2) v2. NOAA, accessed 12 February 2018, https://catalog.data.gov/dataset/2-minute-gridded-global-relief-data-etopo2-v2.

Natoli, M. B., and E. D. Maloney, 2019: Intraseasonal variability of the diurnal cycle of precipitation in the Philippines. *J. Atmos. Sci.*, **76**, 3633–3654, https://doi.org/10.1175/JAS-D-19-0152.1.

——, and ——, 2021: Quasi-biweekly extensions of the monsoon winds and the Philippine diurnal cycle. *Mon. Wea. Rev.*, **149**, 3939–3960, https://doi.org/10.1175/MWR-D-21-0208.1.

——, and ——, 2023: The tropical diurnal cycle under varying states of the monsoonal background wind. *J. Atmos. Sci.*, **80**, 235–258, https://doi.org/10.1175/JAS-D-22-0045.1.

Oh, J.-H., K.-Y. Kim, and G.-H. Lim, 2012: Impact of MJO on the diurnal cycle of rainfall over the western Maritime Continent in the austral summer. *Climate Dyn.*, **38**, 1167–1180, https://doi.org/10.1007/s00382-011-1237-4.

Park, M.-S., C.-H. Ho, J. Kim, and R. L. Elsberry, 2011: Diurnal circulations and their multi-scale interaction leading to rainfall over the South China Sea upstream of the Philippines during intraseasonal monsoon westerly wind bursts. *Climate Dyn.*, **37**, 1483–1499, https://doi.org/10.1007/s00382-010-0922-z.

Peatman, S. C., A. J. Matthews, and D. P. Stevens, 2014: Propagation of the Madden-Julian Oscillation through the Maritime Continent and scale interaction with the diurnal cycle of precipitation. *Quart. J. Roy. Meteor. Soc.*, **140**, 814–825, https://doi.org/10.1002/qj.2161.

——, J. Schwendike, C. E. Birch, J. H. Marsham, A. J. Matthews, and G.-Y. Yang, 2021: A local-to-large scale view of Maritime Continent rainfall: Control by ENSO, MJO, and equatorial waves. *J. Climate*, **34**, 8933–8953, https://doi.org/10.1175/JCLI-D-21-0263.1.

Qian, J.-H., 2020: Mechanisms for the dipolar patterns of rainfall variability over large islands in the Maritime Continent associated with the Madden–Julian oscillation. *J. Atmos. Sci.*, **77**, 2257–2278, https://doi.org/10.1175/JAS-D-19-0091.1.

Rauniyar, S. P., and K. J. E. Walsh, 2011: Scale interaction of the diurnal cycle of rainfall over the Maritime Continent and Australia: Influence of the MJO. *J. Climate*, **24**, 325–348, https://doi.org/10.1175/2010JCLI3673.1.

Riley, E. M., B. E. Mapes, and S. N. Tulich, 2011: Clouds associated with the Madden–Julian oscillation: A new perspective from *CloudSat*. *J. Atmos. Sci.*, **68**, 3032–3051, https://doi.org/10.1175/JAS-D-11-030.1.

Riley Dellaripa, E. M., E. D. Maloney, B. A. Toms, S. M. Saleeby, and S. C. van den Heever, 2020: Topographic effects on the Luzon diurnal cycle during the BSISO. *J. Atmos. Sci.*, **77**, 3–30, https://doi.org/10.1175/JAS-D-19-0046.1.

Ruppert, J. H., Jr., and X. Chen, 2020: Island rainfall enhancement in the Maritime Continent. *Geophys. Res. Lett.*, **47**, e2019GL086545, https://doi.org/10.1029/2019GL086545.

——, ——, and F. Zhang, 2020: Convectively forced diurnal gravity waves in the Maritime Continent. *J. Atmos. Sci.*, **77**, 1119–1136, https://doi.org/10.1175/JAS-D-19-0236.1.

Saito, K., T. Keenan, G. Holland, and K. Puri, 2001: Numerical simulation of the diurnal evolution of tropical island convection over the Maritime Continent. *Mon. Wea. Rev.*, **129**, 378–

400, https://doi.org/10.1175/1520-0493(2001)129<0378:NSOTDE>2.0.CO;2.

Sakaeda, N., G. N. Kiladis, and J. Dias, 2017: The diurnal cycle of tropical cloudiness and rainfall associated with the Madden–Julian oscillation. *J. Climate*, **30**, 3999–4020, https://doi.org/10.1175/JCLI-D-16-0788.1.

——, ——, and ——, 2020: The diurnal cycle of rainfall and the convectively coupled equatorial waves over the Maritime Continent. *J. Climate*, **33**, 3307–3331, https://doi.org/10.1175/JCLI-D-19-0043.1.

Sakurai, N., and Coauthors, 2005: Diurnal cycle of cloud system migration over Sumatera Island. *J. Meteor. Soc. Japan*, **83**, 835–850, https://doi.org/10.2151/jmsj.83.835.

Shige, S., Y. Nakano, and M. K. Yamamoto, 2017: Role of orography, diurnal cycle, and intraseasonal oscillation in summer monsoon rainfall over the Western Ghats and Myanmar Coast. *J. Climate*, **30**, 9365–9381, https://doi.org/10.1175/JCLI-D-16-0858.1.

Short, E., C. L. Vincent, and T. P. Lane, 2019: Diurnal cycle of surface winds in the Maritime Continent observed through satellite scatterometry. *Mon. Wea. Rev.*, **147**, 2023–2044, https://doi.org/10.1175/MWR-D-18-0433.1.

Sobel, A. H., and E. D. Maloney, 2013: Moisture modes and the eastward propagation of the MJO. *J. Atmos. Sci.*, **70**, 187–192, https://doi.org/10.1175/JAS-D-12-0189.1.

Sui, C.-H., and K.-M. Lau, 1992: Multiscale phenomena in the tropical atmosphere over the western Pacific. *Mon. Wea. Rev.*, **120**, 407–430, https://doi.org/10.1175/1520-0493(1992)120<0407:MPITTA>2.0.CO;2.

Vincent, C. L., and T. P. Lane, 2016: Evolution of the diurnal precipitation cycle with the passage of a Madden–Julian oscillation event through the Maritime Continent. *Mon. Wea. Rev.*, **144**, 1983–2005, https://doi.org/10.1175/MWR-D-15-0326.1.

——, and ——, 2017: A 10-year austral summer climatology of observed and modeled intraseasonal, mesoscale, and diurnal variations over the Maritime Continent. *J. Climate*, **30**, 3807–3828, https://doi.org/10.1175/JCLI-D-16-0688.1.

——, and ——, 2018: Mesoscale variation in diabatic heating around Sumatra, and its modulation with the Madden–Julian oscillation. *Mon. Wea. Rev.*, **146**, 2599–2614, https://doi.org/10.1175/MWR-D-17-0392.1.

Virts, K. S., J. M. Wallace, M. L. Hutchins, and R. H. Holzworth, 2013: Diurnal lightning variability over the Maritime Continent: Impact of low-level winds, cloudiness, and the MJO. *J. Atmos. Sci.*, **70**, 3128–3146, https://doi.org/10.1175/JAS-D-13-021.1.

Wang, S., and A. H. Sobel, 2017: Factors controlling rain on small tropical islands: Diurnal cycle, large-scale wind speed, and topography. *J. Atmos. Sci.*, **74**, 3515–3532, https://doi.org/10.1175/JAS-D-16-0344.1.

——, and ——, 2022: A unified moisture mode theory for the Madden–Julian oscillation and the boreal summer intraseasonal oscillation. *J. Climate*, **35**, 1267–1291, https://doi.org/10.1175/JCLI-D-21-0361.1.

Wheeler, M., and H. H. Hendon, 2004: An all-season real-time multivariate MJO index: Development of an index for monitoring and prediction. *Mon. Wea. Rev.*, **132**, 1917–1932, https://doi.org/10.1175/1520-0493(2004)132<1917:AARMMI>2.0.CO;2.

Wu, P., D. Ardiansyah, S. Yokoi, S. Mori, F. Syamsudin, and K. Yoneyama, 2017: Why torrential rain occurs on the western coast of Sumatra Island at the leading edge of the MJO westerly wind bursts. *SOLA*, **13**, 36–40, https://doi.org/10.2151/sola.2017-007.

——, S. Mori, and F. Syamsudin, 2018: Land–sea surface air temperature contrast on the western coast of Sumatra Island during an active phase of the Madden–Julian Oscillation. *Prog. Earth Planet. Sci.*, **5**, 4, https://doi.org/10.1186/s40645-017-0160-7.

Xie, P., R. Joyce, S. Wu, S.-H. Yoo, Y. Yarosh, F. Sun, and R. Lin, 2017: Reprocessed, bias-corrected CMORPH global high-resolution precipitation estimates from 1998. *J. Hydrometeor.*, **18**, 1617–1641, https://doi.org/10.1175/JHM-D-16-0168.1.

Xu, W., and S. A. Rutledge, 2018: Convective variability associated with the boreal summer intraseasonal oscillation in the South China Sea region. *J. Climate*, **31**, 7363–7383, https://doi.org/10.1175/JCLI-D-18-0091.1.

——, ——, and K. Chudler, 2021: Diurnal cycle of coastal convection in the South China Sea region and modulation by the BSISO. *J. Climate*, **34**, 4297–4314, https://doi.org/10.1175/JCLI-D-20-0308.1.

Yanase, A., K. Yasunaga, and H. Masunaga, 2017: Relationship between the direction of diurnal rainfall migration and the ambient wind over the southern Sumatra Island. *Earth Space Sci.*, **4**, 117–127, https://doi.org/10.1002/2016EA000181.

Yang, G.-Y., and J. Slingo, 2001: The diurnal cycle in the tropics. *Mon. Wea. Rev.*, **129**, 784–801, https://doi.org/10.1175/1520-0493(2001)129<0784:TDCITT>2.0.CO;2.

Yokoi, S., S. Mori, F. Syamsudin, U. Haryoko, and B. Geng, 2019: Environmental conditions for nighttime offshore migration of precipitation area as revealed by in situ observation off Sumatra Island. *Mon. Wea. Rev.*, **147**, 3391–3407, https://doi.org/10.1175/MWR-D-18-0412.1.

Zhu, L., Z. Meng, F. Zhang, and P. M. Markowski, 2017: The influence of sea- and land-breeze circulations on the diurnal variability in precipitation over a tropical island. *Atmos. Chem. Phys.*, **17**, 13 213–13 232, https://doi.org/10.5194/acp-17-13213-2017.